Influence of topography and winds on the distribution of water masses on the Antarctic Continental Shelf

Christopher Y. S. Bull[a], David R. Munday[b], Adrian Jenkins[a]

[a] *Department of Geography and Environmental Sciences, Northumbria University, Newcastle upon Tyne, UK.*

[b] *British Antarctic Survey, Cambridge, United Kingdom.*

Corresponding author: Christopher Y. S. Bull, christopher.bull@northumbria.ac.uk

File generated with AMS Word template 2.0

ABSTRACT

Central to improving our understanding of ocean temperature change on Antarctica's continental shelf is a better understanding of how the ocean circulation drives the onshore flux of warm deep waters across the shelf break. This study uses a primitive equation ocean model to explore how the circulation regime and changes in surface stress influence the temperature structure on Antarctica's shelf seas. As the shelf temperature changes are largely driven by ocean circulation changes, understanding these becomes our focus. A simple barotropic model is used to describe the linear theory of the difference between throughflow and gyres regimes, and their expected response to changes in forcing. This theory informs our understanding of the barotropic circulation response of the primitive equation model where a momentum budget confirms that over the simulated equilibrated timescales with surface forcing changes, the response is first-order linear. Consistent with previous findings, we find that climate change projection-like wind shifts (stronger westerlies that shift south) have a direct influence on Ekman processes across the shelf break and upwell warmer waters onto the shelf. We also find that the circulation regime (throughflow or gyre -- determined by basin geometry), influences the mean shelf temperature and how susceptible the existing shelf temperatures are to changes in surface stress. While the throughflow regime can experience a complete transition in on-shelf temperatures when the transition between westerly and easterly winds shifts southward, we find relatively modest bottom intensified warming at the Ice Front in a gyre regime.

SIGNIFICANCE STATEMENT

The Antarctic Slope Front determines how much warm water flows onto the shelf and the subsequent heat that is available to melt the ice shelves. This study explores the impact of basin geometry and wind shifts on the large-scale ocean circulation around Antarctica's continental shelf with a focus on understanding changes in shelf temperature near an imagined Ice Front. Here, meridional topographic barriers change geometry, shedding insight into how different water temperatures on the shelf coalesce despite having the same initial conditions and wind forcing. Wind perturbation simulations suggest why some regions are more sensitive to shifts in winds than others. These findings highlight an underappreciated yet fundamentally important topographical constraint under future changes in winds.

File generated with AMS Word template 2.0

1 Introduction

In their canonical form, a circumpolar-like throughflow (e.g. Antarctic Circumpolar Current -- ACC) and an ocean gyre (e.g. Weddell gyre) can be created in an open re-entrant channel and a closed box by blowing a uniform wind and a half cosine wind, respectively. In the re-entrant channel case (hereafter, "throughflow regime"), a uniform eastward wind drives an eastward current. Eddy saturation aside, increasing the strength of the wind uniformly, might be expected to drive a stronger eastward current. The closed box (hereafter, "gyre regime") analogue feels like a paradox in comparison; adding a uniform wind to the half cosine wind, does not strengthen the circulation (Hughes, 1997). This is because the circulation depends on the wind stress curl, here, the meridional gradient of zonal velocity and thus a uniform change in wind does not change the horizontal circulation (Veronis, 1996). In a throughflow regime, e.g., a re-entrant channel with a flat bottom, a momentum budget reveals a primary balance between zonal momentum input from the wind balanced by bottom friction which results in an unrealistically strong ACC and a large SSH gradient (Hidaka & Tsuchiya, 1953; D. R. Munday et al., 2015; Olbers et al., 2007). *Munk and Palmen* (1951) showed that in the presence of significant bathymetry, topographic form stress (as it is now known) is a more effective sink of momentum, slowing down the eastward flow and creating an abyssal bottom geostrophic return flow that is confined to the height of the bathymetry. In contrast, in the closed box, the insightful perspective (Hughes, 1997; Olbers, 1998; Styles et al., 2021) is taken via the curl of the momentum equation, whereby a vorticity budget reveals a primary balance between the curl of the wind stress acting as a source of vorticity and the curl of the bottom friction (flat bottomed) or the curl of the topographic form stress (significant bathymetry) acting as a vorticity sink. This profound importance of boundary conditions has led to the tendency to focus on these distinct dynamical balances when studying throughflows as compared to gyres. As the real system exhibits both kinds of flows, we need a better understanding of the transitory dynamics of these two regimes so we can better predict how they will change as there forcing evolves with climate change.

In the real Southern Ocean (Figure 1a), the ocean circulation exhibits mixtures of both throughflow and gyre regimes. The zonal wind and sea-ice stress determine the momentum input driving the ocean circulation (Figure 1b). Our throughflow regime currents are the eastward flowing Antarctic Circumpolar Current (ACC) and a shelf confined westward flow

File generated with AMS Word template 2.0

that is effectively a combination of the Antarctic Slope Current (ASC) and the Antarctic Coastal Current. Note that the ASC is not quite a circumpolar feature; it is not found along the western Antarctic peninsula where the ACC flows along the continental slope (Thompson et al., 2018; Whitworth et al., 1998). Our gyre regimes, formed through steep f/h contours (Olbers et al., 2007; Patmore et al., 2019; Wilson et al., 2021), are the clockwise flowing Weddell, Ross and Australian-Antarctic gyres. The ACC is predominantly driven by wind and buoyancy forcing and is the world's strongest current (Olbers et al., 2012); modern estimates of Drake Passage transport vary between 137±7Sv (thermal wind only; *Meredith et al.*, 2011) and 173.3 for total transport (Donohue et al., 2016). Several studies in realistic settings (e.g. *Masich et al.*, 2015) have confirmed that topographic form stress is the dominant sink of momentum. At the coast, ice shelves flow from the ice sheet and are vulnerable to future changes in sub-surface ocean temperatures.

File generated with AMS Word template 2.0

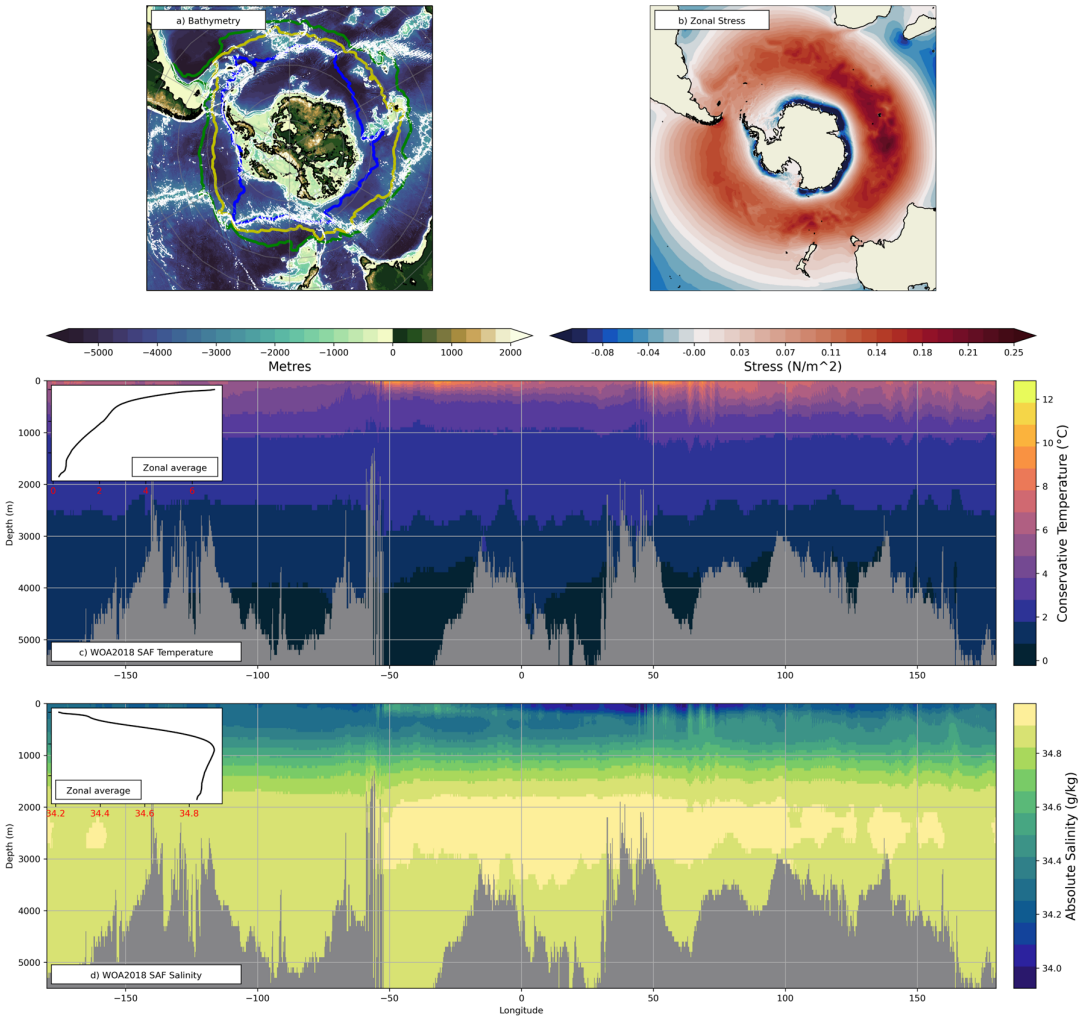

Figure 1. a) ETOPO1 bathymetry, thick contours indicate Southern Boundary (blue), Polar Front (yellow), and Subantarctic Front (green) from *Park et al.* (2019); thin white contours highlight -3000, -2000, -1000 isobaths, and black is the surface land mask. b) JRA zonal stress (time-mean 1986-2000; both wind and sea ice). WOA2018 Subantarctic Front (green contour in panel a): c) Temperature and d) Salinity. The insets in c-d show the zonal average of temperature and salinity, respectively; these T/S profiles are used as initial and northern boundary restoring conditions for the modelling configuration in this study (see Section 2b).

The Antarctic Slope Front (ASF) is a landward thickening of the layer of cold surface waters that, through its position on the continental shelf break, regulates onshore heat transport associated with inflow of warmer sub-surface waters. In the case of the Weddell and Ross gyres, the related ice shelves experience low melt rates because warm water has limited direct access to the ice-shelf base. Much of the recent interest in the ASF (Thompson et al., 2018) is due to its capacity to modulate the inshore flux of Circumpolar Deep Water melting the ice shelves. The ASC is mainly driven by the along slope westward wind stress

File generated with AMS Word template 2.0

(Pauthenet et al., 2021; Thompson et al., 2018) whereas the Weddell and Ross gyres with transports 30-100 and 23±8 Sv (respectively) are sensitive to local changes in wind stress curl (Armitage et al., 2018; Dotto et al., 2018; Gómez-Valdivia et al., 2023; Neme et al., 2021). The winds over the southern ocean vary on several timescales and all of these current systems are expected to show some sensitivity to the projected southward shift in winds (e.g. Bracegirdle et al., 2013; Goyal et al., 2021) although a signal has not necessarily been observed (e.g. Armitage et al., 2018; Stewart, 2021).

Considerable work has gone into understanding the anticipated changes in Southern Ocean circulation as a result of changes in the westerly winds (e.g. Farneti et al., 2015; David R. Munday et al., 2013; Purich & England, 2021; Spence et al., 2017). Substantial work has gone into characterising eddy saturation of the ACC (Gnanadesikan & Hallberg, 2000; Straub, 1993; Tansley & Marshall, 2001), eddy saturation is reached when the ACC's total transport becomes insensitive to surface forcing stress changes. Despite the total transport not changing, we would expect the barotropic transport to respond to changes in surface forcing in a near linear way (Constantinou & Hogg, 2019). Using a more realistic configuration, *Spence et al.* (2014) has shown that anticipated southward shifts in the southern ocean winds lead to a change in Ekman dynamics at the coast. Specifically, reduced Ekman pumping at the coast leads to a flattening of isotherms, enabling increased inflow of warm waters onto the shelf. Whilst it is tempting to apply these arguments around all of Antarctica, some regions are more susceptible to these shifts than others (Verfaillie et al., 2022). Under a uniform 4° shift, the Amundsen Sea warms the most whereas the Ross Sea cools and the Weddell Sea shelf modestly warms (Figure S5b in *Spence et al.* (2014)). Now, recall that meridionally uniform changes to the winds would not be expected to change the horizontal circulation of a gyre regime but would have a strong response in a throughflow regime (Olbers, 1998; Vallis, 2017; Veronis, 1996). As described above, the work to date has focused on wind shifts that assume a channel-like regime which suggests that we might be over-estimating the effect. A natural question arises: given the projected wind changes are similar to a positive constant offset in the winds (westerly strengthening and southward shift), how do we expect the Southern Ocean to respond in places where there are a mixture of throughflow and gyre regimes?

File generated with AMS Word template 2.0

The goal of this study then is to re-visit channel and gyre regimes in the context of an idealised Southern Ocean configuration with southward (uniform offset) wind shift experiments. Practically, the community, for the purpose of attribution, needs to understand the implications of a change in wind strength, shifts and curl change; using uniform offsets makes progress towards disentangling these issues. We will use barotropic linear theory to better understand *how* a uniform change in stress is so important in a throughflow regime but not in a gyre regime system, and via a primitive equation ocean model, how the system is complicated by a shelf with baroclinicity. Whilst the integrated changes in horizontal circulation from a re-entrant channel to a hard wall are well known (e.g. Olbers, 1998; Tansley & Marshall, 2001; Vallis, 2017), we believe this is the first time an incremental mixture of these two regimes has been studied in terms of wind shifts and the temperature structure on the shelf. Two questions arise:

1. Subject to the same starting point, how are the mean shelf temperatures influenced by a hierarchy of basin geometries?

2. How is basin geometry important for modulating shelf temperature changes with shifts in the winds?

The paper is presented as follows: linear theory is explored in Section 2. Followed by the numerical model description, experiment design and results in Sections 3.1, 3.2, 4, respectively. A summary and discussion is given in Section 5.

2 Southern Ocean circulation theory: throughflow versus gyre regimes

Figure 2 utilises the *Stommel* (1948) planetary geostrophic equations to highlight throughflow and gyre circulations within an idealised, barotropic, flat-bottom configuration and rigid lid. The idea of using this simple model is that it offers a heuristic, setting our theoretical barotropic expectations for what may happen in a more complex primitive

File generated with AMS Word template 2.0

equation ocean model with baroclinicity and a shelf (Section 4). Our 2D, non-dimensionalised[1] equations are:

$$f\boldsymbol{k} \times \boldsymbol{u} = -\nabla p - r\boldsymbol{u} + \tau_x$$

$$\nabla \cdot \boldsymbol{u} = 0$$

where f is the Coriolis parameter – negative for the Southern Ocean, $\boldsymbol{u}$ is a two-dimensional velocity vector, p is pressure, r is a friction coefficient, τ_x a zonal stress and ∇ operates horizontally. A zonal surface stress, inspired by the observed pattern (Figure 1) is used. Hereafter, 'surface stress' and 'wind stress' will be used interchangeably. Compared to previous Southern Ocean idealised studies (e.g. *Abernathey et al.* (2011)), the wind stress here includes Easterlies and has a non-zero stress in the South where we imagine an ice shelf front. A change in the boundary condition, from a re-entrant east-west channel to a wall, leads to fundamental changes in the circulation. Heuristically, we discuss throughflow and gyre regimes in terms of the pictured layers: top ($-\tau_x/f$) and bottom Ekman ($r\boldsymbol{u_{geo}}/f$) layers, and geostrophic transports ($-\nabla p/f$). Note that, here, all 3 layers are really taking place in one slab of fluid and the transports in the pictured layers are diagnostic. In contrast, in the z-level primitive equation model in Section 4, they will be separated by depth and solved using a depth-dependent momentum equation. This approach is used because it highlights the linear dynamics relevant to our wind shift experiments in Section 4 and shows how a prescribed wind stress sets up the circulation in the lower layers.

[1] The dimensionalised form, with reference density ρ_0 and ocean depth H is: $H(f\boldsymbol{k} \times \boldsymbol{u}) = -H(\frac{1}{\rho_0}\nabla p) - r\boldsymbol{u} + \frac{\tau_x}{\rho_0}$ and $H(\nabla \cdot \boldsymbol{u}) = 0$. To non-dimensionalise (around r), parameters ρ_0 and H are set to 1.

File generated with AMS Word template 2.0

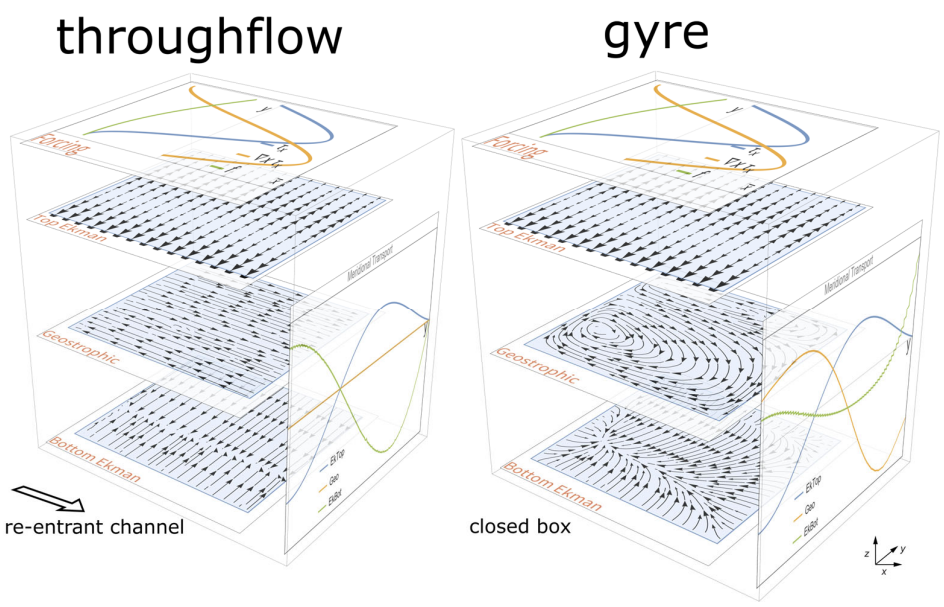

Figure 2. Comparison of throughflow (left) and gyre (right) regimes for an idealized Southern Ocean wind stress in a single-layer ocean. The channel has a re-entrant east-west boundary whereas the gyre has walls on all sides. Horizontal layers show the forcing, Ekman and Geostrophic layers. The "forcing" layer shows the zonally averaged wind stress, wind stress curl and Coriolis parameter. The circulation layers are: top Ekman, geostrophic and bottom Ekman transports, respectively; the barotropic streamfunction is the sum of the three layers. The vertical panel shows the zonally averaged meridional transport for each component.

a. Commonalities and differences to both throughflow and gyre regimes.

As pictured in Figure 2, in both throughflow and gyre regimes, the top (near surface) Ekman transport is the same. In the Southern hemisphere, the top Ekman transport is directed 90° degrees to the left and surface Ekman suction and pumping arises due to divergences and convergences (respectively) in the near-surface Ekman transport. Here, a change from cyclonic to anti-cyclonic wind stress curl leads to a change from upwelling to downwelling regions either side of the maximum westerlies. We thus expect upwelling South of the peak westerlies and downwelling to the North. Relatedly, approaching the boundaries for the 'control' wind stress shown, the curl goes to zero in the South but is non-zero in the North, hence, only the Northern boundary will have curl driven downwelling. Confounding matters, we have no normal flow conditions at the Southern and Northern boundaries. For the wind stress shown, at the Southern wall, we have a non-zero Easterly wind which is incompatible with the boundary condition so by continuity leads to downwelling. In contrast, the Northern wall goes to zero stress and so the wind *at the boundary* does not drive 'continuity driven' downwelling. We will return to these ideas when considering wind shifts.

File generated with AMS Word template 2.0

In a throughflow regime, the top Ekman transport leads to a meridional pressure gradient that drives geostrophic currents that match the wind direction (Figure 2 throughflow, geostrophic layer), this is enabled by the re-entrant boundary. The bottom Ekman transport then flows to the right of the geostrophic transport returning the flow transported by the top Ekman layer (Figure 2 throughflow, meridional transport panel). Here, a Stommel linear friction is used so the bottom Ekman transport is 90° degrees to the right of the geostrophic transport (rather than 135° for the Ekman solution; *Olbers et al.* (2012)). Thus, in a zonally averaged throughflow regime, we have a clockwise and anti-clockwise overturning cell where the latitude of zero wind stress, delineates the boundary between the two cells that are driven by the Westerly and Easterly winds, respectively.

In a gyre regime, the no normal flow condition of the eastern and western boundaries results in dramatic changes. In the geostrophic layer, the depth-integrated circulation consists of a balance between the meridional advection of planetary vorticity and the wind stress curl (i.e. Sverdrup balance); in the return flow boundary layer, the advection of planetary vorticity is balanced by the curl of bottom friction. Here, the top Ekman transport is prescribed, this sets off a top Ekman pumping and suction pattern that is now constrained by walls on all sides. Since the geostrophic flow is largely horizontally non-divergent, Ekman pumping/suction through the top and bottom Ekman layers results in stretching and squeezing of fluid columns in the geostrophic layer. The circulation is further constrained: the sum of the Ekman and geostrophic components gives the depth-integrated transport where the bottom Ekman transport is 90° degrees to the right of the geostrophic transport. Unlike in a throughflow regime, a gyre regime has geostrophic zonal and meridional flows that are non-uniform in x. Also unlike in a throughflow regime, the meridional return transport is no longer confined to the bottom Ekman layer but also to the geostrophic return flow (Figure 2 gyre, meridional transport panel). This is because in a throughflow regime, there is no western wall to support a pressure gradient and so there can be no geostrophic meridional transport.

b. Linear responses of both systems to wind shifts.

We consider a constant positive, zonally uniform change in wind stress called “c”. This change only offsets the pictured Figure 2 wind profile and so aside from at the boundaries, the wind stress curl does not change. In an idealised sense, this is similar to what we expect

File generated with AMS Word template 2.0

with climate change; an increase in the strength of the westerly winds, a weakening of the easterlies and a shift of the easterly-westerly transition zone south. Changes in the top Ekman layer are common to both regimes, but the means in which the lower layers balance the momentum input is different due to the change in boundary condition. In a throughflow regime, as "c" increases, the north-south sea surface height gradient associated with the zonal geostrophic flow gets stronger and so it directly modifies the strength of the zonal geostrophic currents. In a gyre regime however, the *zonal* Sverdrup transport is related to *the gradient* in the wind stress curl, and thus the zonal transport is locked. In both regimes, away from boundaries, the curl is not changing so neither can the region or magnitude of upwelling and downwelling. The magnitude of Ekman transport does change, so by continuity, the downwelling transport at the northern and southern boundaries has to change, and in this instance an increase in one leads to a compensating decrease in the other.

In a throughflow regime, the eastward and westward jets associated with the eastward and westward stresses increase and decrease in strength (respectively). With positive c, as the geostrophic eastward jet accelerates the bottom Ekman transport also increases. Most importantly, the two Ekman overturning cells described earlier in this Section shift south. Since the latitude of the easterly-westerly transition zone has shifted south, the upwelling of the northern cell has also shifted south; this change will be a crucial feature in our numerical experiments in Section 4. So how is it that a change in surface stress can have such a dramatic effect in a throughflow regime as compared to a gyre?

Veronis (1996) and *Vallis* (21.7.6; 2017) provide some clues for how we can understand the gyre regime response. As a heuristic, consider a closed box with a uniform, zonal, eastward wind and a free surface. This sets up a northward Ekman transport which then drives an eastward geostrophic current. The eastward geostrophic current creates a raised sea

File generated with AMS Word template 2.0

surface height in the east, driving a geostrophic current southward[2]. Bottom Ekman transport aside, this geostrophic current returns the volume displaced by the original northward Ekman transport. At equilibrium, there is no zonal flow but there is a west-east gradient in sea surface height and a meridional overturning circulation with northward transport in the surface Ekman layer and a southward return flow in the geostrophic interior. Moreover, if we now uniformly increase the strength of the wind, at equilibrium, we only expect an increase in the gradient of sea surface height (21.7.6 in *Vallis* (2017)) and an associated increase in the meridional overturning. Returning to the wind and layered box in Figure 2, since the total circulation streamfunction is determined by the curl of the stress and our constant offset c has no curl, it does not change the total streamfunction. Exploiting our simple previous example, the sea surface height gradient *change* only depends on the sign of c, not on the direction of the winds. Moreover, for the total streamfunction to not change, the vertical structure of the flow has to compensate via a change in upwelling or downwelling at the northern and southern walls.

Veronis (1996) shows that a constant offset of the stress effects both the Ekman and geostrophic transports in a compensating manner, whilst very large offsets are explored we will consider smaller changes in this study. *Veronis* (1996) suggests that the compensation occurs equally between geostrophic and a top Ekman component, bottom Ekman is not considered. Here, we also consider changes in the bottom Ekman layer as they are important for how deep, relatively warm waters get up and across the shelf break, this means that any changes in the top Ekman transport driven by c, needs to be compensated by a change in the geostrophic transport *and* bottom Ekman transport (driven by changes in the geostrophic transport). Since the zonal Sverdrup transport is related to the gradient in the wind stress curl and here, we only have zonal winds, the geostrophic compensation will occur in the meridional transport. In Figure 2, right panel, imagine adding a constant offset c: as the top

[2] In contrast, in the throughflow case, the increased zonal momentum input is balanced by stronger bottom friction.

File generated with AMS Word template 2.0

Ekman transport moves uniformly up the geostrophic transport will uniformly shift down (Stommel, 1957) to compensate. In the meridional average (not shown), the southward meridional geostrophic transport gets stronger with constant offset c. The consequences of this simple linear theory will now be explored in a primitive equation ocean model.

3 Model and experimental design

a NEMO model configuration

The ocean general circulation model used in this study is version 4.0.4 of the Nucleus for European Modelling of Ocean model (NEMO; *Gurvan et al.* (2017)). NEMO solves the incompressible, Boussinesq, hydrostatic primitive equations with a split-explicit free-surface formulation. NEMO here uses a z*-coordinate (varying cell thickness) C-grid with partial cells at the bottom-most and top-most ocean layers in order to provide more realistic representation of bathymetry (Bernard et al., 2006) and the ice-shelf geometry, respectively. Our model settings include: a 55-term polynomial approximation of the reference Thermodynamic Equation of Seawater (TEOS-10; IOC and IAPSO (2010)), nonlinear bottom friction, a free-slip condition at the lateral boundaries (at both land and ice shelf interfaces), energy- and enstrophy-conserving momentum advection scheme and a prognostic turbulent kinetic energy scheme for vertical mixing. Laterally, we have spatially varying eddy coefficients (according to local mesh size) with a Laplacian operator for iso-neutral diffusion of tracers and a biharmonic operator for lateral diffusion of momentum.

Symbol	Value	Description
L_x, L_y	2003.7, 3025	Domain size
H	3047 m	Depth of domain
Δ_x, Δ_y	7.9 km	Horizontal resolution
Δ_z	68 m	Vertical resolution
f_0	$-1.46 * 10^{-4}$	Southern boundary Coriolis
f_y	$-1.28 * 10^{-4}$	Northern boundary Coriolis
L_{EW}	770 km	Value of x where winds transition from easterly to
$L_{easterlies}, L_{westerlies}$	385, 2239 km	Distance over which the easterly and westerly
τ_E, τ_w	-0.05, 0.2 N	Peak easterly and westerly wind stress

Table 1. Key parameters used in the configuration with model reference winds (τ_0).

File generated with AMS Word template 2.0

303

304 The modelling setup is pictured in Figure 3 with key parameters in Table 1. The
305 modelling domain is on a β-plane with 257 x 385 regularly spaced points in x and y,
306 respectively. The ocean floor is limited to 3023 m and is represented by 45 vertical levels.
307 Walls exist on the northern and southern boundaries where the external forcing is a restoring
308 condition at the northern boundary and a surface wind stress (Figure 3), where the restoring is
309 towards the initial state. The western-eastern boundary is re-entrant, Figure 3 however is
310 effectively in a gyre regime due to a wall at 86 km. The simulations are initialised from rest
311 with initial conditions (Figure 1 insets), these fields then also set the northern restoring
312 condition as the simulation evolves. The configuration has no: ice-shelf, sea ice and tides, but
313 is inspired by previous southern ocean idealised channel modelling (e.g. (Abernathey et al.,
314 2011; Morrison et al., 2011)), where the interest here was to have a simple system in which to
315 understand the momentum balance's role in setting shelf properties from wind stress forcing
316 alone. All simulations in this paper have a spin-up of 90 years where the time-mean values of
317 a further 10 years are used for all analysis. Spin-up metrics including domain averaged SSH
318 and domain integrated salinity, temperature and kinetic energy, combined with test
319 simulations of 370 years, suggest that the 90 year spin-up is sufficient to capture the
320 equilibrated response of the ocean circulation to the forcing.

File generated with AMS Word template 2.0

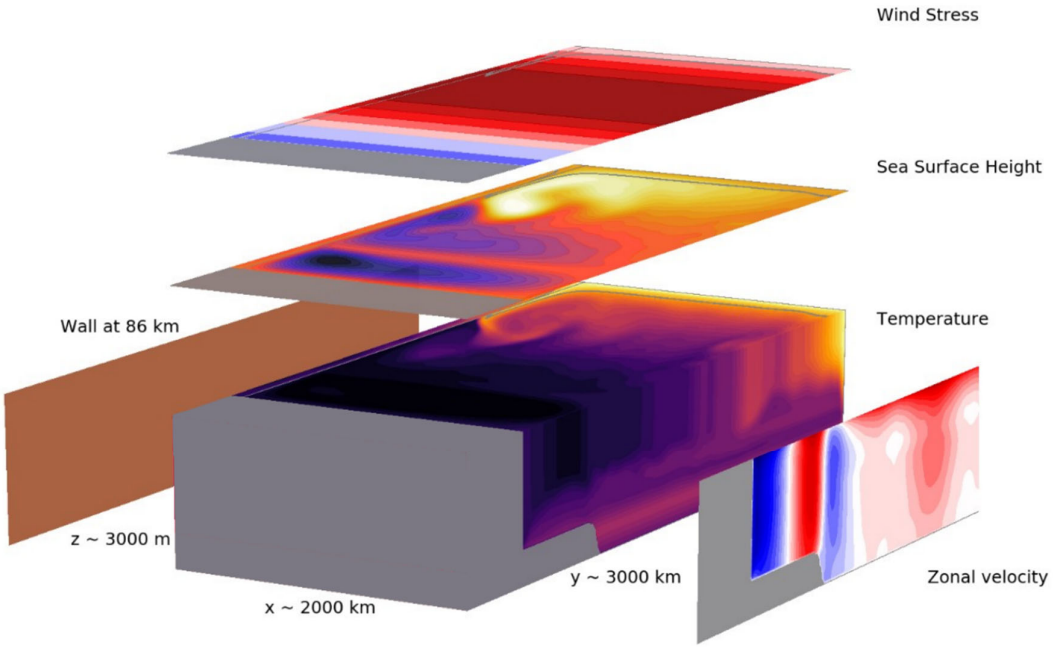

Figure 3. A 3D snapshot of the model's temperature field from a gyre experiment. The temperatures range from -1.9 to 1.5 °C. Overlaid, above: sea surface height (-5 to 20 cm) and the control wind stress (τ_0; -0.05 to 0.2); right: zonal mean zonal velocity (-20 to 20 cm/s); left: most experiments have some kind of wall at 86 km, here, there is a wall the full length of the domain.

b Experiment design

1) SURFACE FORCING AND BATHYMETRY

Given the idealized nature of this study, we choose an idealized surface forcing and boundary conditions. The wind stress forcing is the same zonally throughout the domain (meridional wind stress is zero) and is intended to represent a zonal average of the Southern Ocean's easterlies and westerlies (Figure 1b):

$$\tau_c(y) = \begin{cases} 0, 0 < y < 393\ km \\ \tau_E * \sin\left({}^{-0.5\,\pi y}/_{L_{easterlies}}\right) + c,\ 393 \leq y \leq 770\ km \\ \tau_W * \sin\left({}^{\pi y}/_{L_{westerlies}} - {}^{L_{EW}\pi}/_{L_{westerlies}}\right) + c,\ 770 \leq y \leq 3025\ km \end{cases}$$

$c = 0$ is the control simulation (τ_0). Four additional values of c give the four perturbation forcings: $\tau_{-0.1}$, $\tau_{-0.05}$, $\tau_{0.05}$, $\tau_{0.1}$. The wind stress fields used are shown graphically in Figure 4a. To emulate the geometry of the Southern Ocean (see Figure 1a and Section 1 discussion),

File generated with AMS Word template 2.0

we then have four different bathymetries (Figure 4 middle and bottom row). All bathymetries have the same common sea floor and shelf (gray line Figure 4a) that is zonally uniform. The first case (δ_{NONE}) only consists of this zonally uniform sea floor and shelf, whereas cases 2-4 (δ_{swall}, δ_{oowall}, δ_{wall}) have a wall at 86 km that is a single grid cell wide. Since the western-eastern boundary is re-entrant, the construction of a wall is effectively changing the boundary condition. Thus, in the case of δ_{NONE} we are in a throughflow regime and in δ_{wall} gyre regime.

File generated with AMS Word template 2.0

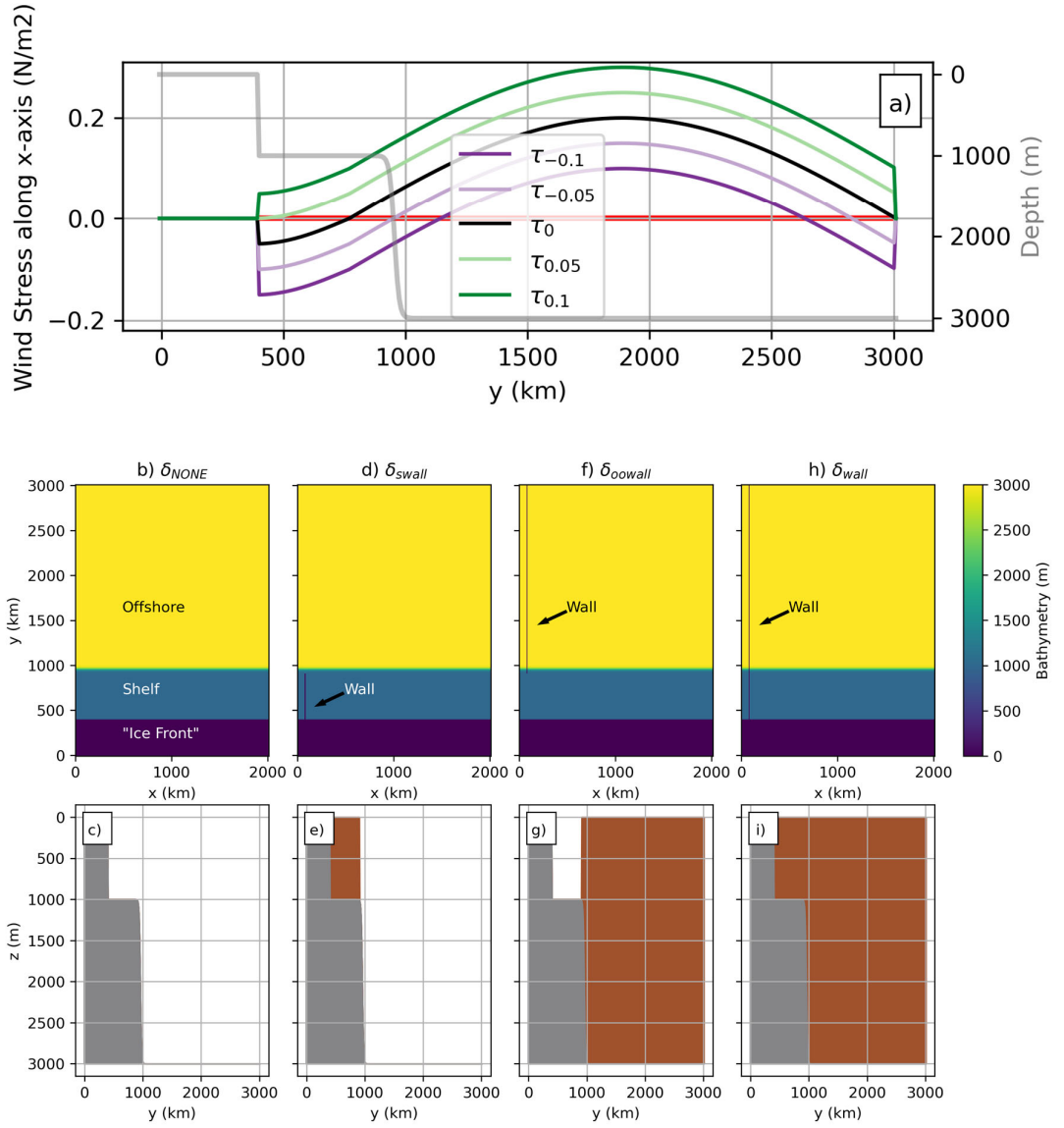

Figure 4. a) Five zonally uniform wind stress forcings applied to each of the 4 bathymetries (lower panels); black (τ_0) is the control simulation and perturbation experiments are created by adding ($\tau_{.05}$, $\tau_{.1}$) or removing ($\tau_{-.05}$, $\tau_{-.1}$) a constant. Red horizontal line at zero highlights transition from easterlies to westerlies, where applicable. Gray line (twin axis, scale on right) shows the bathymetry common to all experiments (i.e. δ_{NONE}). Middle and bottom rows show the 4 different bathymetries (δ_{NONE}, δ_{swall}, δ_{oowall},δ_{wall}) used to create different "boundary conditions". b-i) Prescribed bathymetry used for experiments 1-20 experiments (surface forcing shown in Figure 1), each column is a new bathymetry. Middle row: plan view. Bottom row: meridional slice where gray shows the bathymetry (unchanged across all bathymetries) and brown shading (b-d) shows the wall at x = 86 km (approx). All experiments are listed in Table 2.

2) Experiments

From Figure 4, we have five different surface forcings (Figure 4a; $\tau_{-0.1}$, $\tau_{-0.05}$, τ_0, $\tau_{0.05}$, $\tau_{0.1}$) and four different bathymetries (Figure 4 middle and bottom row; δ_{NONE}, δ_{swall},

359 δ_{oowall}, δ_{wall}), taking the combinations leads to 20 experiments (Table 1). The simulations
360 are designed to highlight the dependence of the strength and location of the ASF to changes
361 in boundary condition and changes in surface forcing.

362

Number	Name	Boundary condition is				Surface Forcing (c)
		Fully Open	Shelf Block	Deep Ocean Block	Fully Closed	
1	$\delta_{NONE}\tau_{-0.1}$	✓				-.01
2	$\delta_{NONE}\tau_{-0.05}$	✓				-0.05
3	$\delta_{NONE}\tau_{0}$	✓				0
4	$\delta_{NONE}\tau_{0.05}$	✓				.05
5	$\delta_{NONE}\tau_{0.1}$	✓				.1
6	$\delta_{swall}\tau_{-0.1}$		✓			-.01
7	$\delta_{swall}\tau_{-0.05}$		✓			-0.05
8	$\delta_{swall}\tau_{0}$		✓			0
9	$\delta_{swall}\tau_{0.05}$		✓			.05
10	$\delta_{swall}\tau_{0.1}$		✓			.1
11	$\delta_{oowall}\tau_{-0.1}$			✓		-.01
12	$\delta_{oowall}\tau_{-0.05}$			✓		-0.05
13	$\delta_{oowall}\tau_{0}$			✓		0
14	$\delta_{oowall}\tau_{0.05}$			✓		.05
15	$\delta_{oowall}\tau_{0.1}$			✓		.1
16	$\delta_{wall}\tau_{-0.1}$				✓	-.01
17	$\delta_{wall}\tau_{-0.05}$				✓	-0.05
18	$\delta_{wall}\tau_{0}$				✓	0
19	$\delta_{wall}\tau_{0.05}$				✓	.05
20	$\delta_{wall}\tau_{0.1}$				✓	.1

363 Table 2. List of Experiments. Name indicates the bathymetry (δ) and surface forcing (τ_c) used. A red
364 tick highlights the experiment which uses the control forcing (τ_0) in each bathymetry. See Figure 1 for
365 details.
366

File generated with AMS Word template 2.0

4 Numerical Results

a Summary of mean state circulation for throughflow and gyre regimes.

Figure 5 shows mean circulation metrics of the two "bookend" cases with a control surface stress, namely, $\delta_{NONE}\tau_0$ which is in a fully throughflow regime and $\delta_{wall}\tau_0$ which is in a gyre regime. Comparing Figure 5a,f the throughflow case has a strong temperature front and relatively cold waters towards the southern boundary, in the gyre case on the shelf, the isotherms form an inverted bowl with a small dip of colder waters at the shelf break forming the well-known v-shaped front (Thompson et al., 2018). The circulation metrics in the subsequent columns are broadly consistent with the linear circulation response discussed in Section 2, with the addition of more complex physics and the addition of a shelf. The barotropic streamfunction in Figure 5d,i gives a circulation that is consistent with linear theory from Section 2a. In Figure 5b,d, like Figure 2, we see a zonal flow that matches the wind direction, due to a flat bottomed deep ocean the transports are very large. In Figure 5i, the addition of a shelf introduces steep f/h contours, leading to an additional gyre in the south (same direction as the curl is unchanged over that region). Figure 5i also has non-linear, eddy features (standing eddies, meanders and eddy-recirculation) in-between the two large gyres due to vorticity transport (Stewart et al., 2021). Comparing Figure 5b,g, the additional zonal flows in Figure 5g are consistent with the three gyres observed in Figure 5i. Looking at the meridional velocities in Figure 5c,h, transport in the top and bottom Ekman layers is also consistent with Section 2a; in particular, the change of direction in the top and bottom layers in a throughflow regime coincides with the change in the wind direction. As expected, in a throughflow regime, the return flow is confined to a bottom Ekman layer whereas in a gyre regime the geostrophic return flow is higher in the water column. Combining these perspectives we can consider the overturning streamfunction, for a throughflow regime (Figure 5e), we have a clockwise and anti-clockwise overturning cells which are separated by the change in wind direction. For a gyre regime (Figure 5j), two similar cells are much closer to the surface and we have an additional 3 sub-surface cells that arise from the change in zonal currents (Figure 5g). Consideration of how temperature on the shelf and the overturning changes in terms of the experiments in Table 2 (Figure 11) is a key objective of this study.

File generated with AMS Word template 2.0

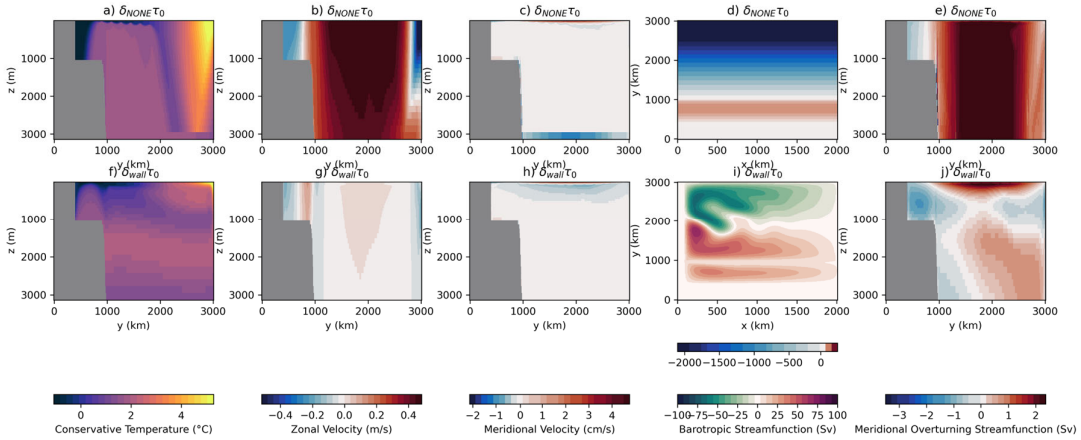

Figure 5. Overview of the mean state of the open (first row; δ_{NONE}) and closed channel (second row; δ_{wall}) with control wind stress (τ_0). Along the columns: Conservative Temperature (°C), Zonal Velocity (m/s), Meridional Velocity (cm/s), Barotropic Streamfunction (Sv) and Meridional Overturning Streamfunction (Sv) where the first 3 are the zonal average. To compensate for very large transports, rows 1-2 have a different colourbar for the Barotropic Streamfunction.

b Shelf temperatures are modulated by winds and circulation regime

Figure 6-7 are the main results in this study that we wish to explain through subsequent analysis; Figure 6 shows the zonal average and the response of the ASF whereas Figure 7 highlights the heat that is available on the southern boundary to be fluxed into an imagined ice shelf (not represented here). Figure 6 shows that there are two mechanisms by which the strength and structure of the warm waters on the shelf can be altered, by shifting the winds (Figure 6 columns) or by creating a gyre via a change in the boundary constraint (Figure 6 rows). Looking down any Figure 6 column where the coastal downwelling is fixed, we note that the boundary constraint is a key factor in determining the intensity and location of the ASF. For example, focusing on the central column (control wind stress; τ_0), the warmest waters reach the southern boundary when the shelf has a wall (Figure 6h) whereas the presence of a deep ocean gyre, reduces the temperature of warm waters in the slope current on the shelf (Figure 6c,m). Additionally, the winds are another key constraint, looking left to right *across the rows*, a southward shift in the transition zone from westerlies to easterlies increases the intensity of warm waters on the shelf. This shift is most effective, however, when the winds are shifted over an open channel region (Figure 6 rows 1-3) where the northern Ekman overturning cell's upwelling region is shifted south of the shelf break. In short, the presence of a wall increasingly hinders the capacity of the winds to drive warmer waters across the shelf and so the winds are maximally effective in a fully throughflow regime (Figure 6a-e; δ_{NONE}). The other extreme then, is the introduction of a full north-south

File generated with AMS Word template 2.0

wall (Figure 6 row 4; δ_{wall}) where changes in the winds are no longer able to (dramatically) change the intensity and location of the ASF. This is due to there being no change in the (total) horizontal circulation in the presence of a wall because, by design, changes in τ_c do not (generally) change the wind stress curl, how this is achieved baroclinically is discussed in Section 4c. Finally, a wall in the deep ocean (Figure 6 row 3; δ_{oowall}) flattens isotherms in the deep ocean thus reducing the amount of available heat close to the shelf break to be brought up onto the shelf when the winds are shifted.

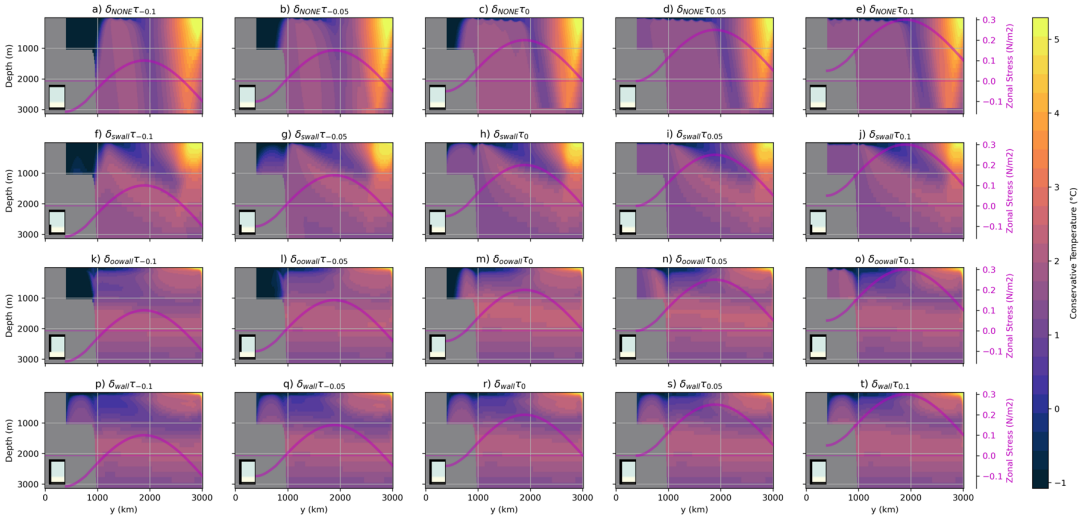

Figure 6. Zonal mean temperature for all experiments (Table 2). Each column has a new wind stress forcing (Figure 4a) where the middle column is the control wind stress. The magenta line highlights the zonally averaged wind stress. Each row has a different boundary condition, in order: i) fully re-entrant, ii) blocked shelf, iii) blocked deep ocean and iv) fully blocked shelf and deep ocean, respectively. The small glyphs (bottom-left) schematically indicate the geometry under consideration in each panel. This panel-experiment layout applies to Figures 6-8, 10-11 and S1-S5.

Sub-surface temperature changes at our imagined ice front are particularly relevant to ice shelves, Figure 7 then refines our focus towards the zonal temperature changes at the southern boundary. Due to the presence of a wall and changes in top-layer Ekman transport, we do expect and observe differences in downwelling at the southern boundary (e.g. Figure 7g-h). Figure 7 highlights the importance of identifying when a region is in a gyre regime (boundary condition). Comparing rows, the shelf gyre is important by the warmer ice front temperatures in Figure 7g,h as compared to the runs without a wall on the shelf (Figure 7b,c,l,m). In these instances, the wall on the shelf provides the most effective transport of shelf edge temperatures to the ice front by enhancing the cross-shelf transport of waters, only in the presence of a wall is there any meridional geostrophic flow. When the shelf is open

File generated with AMS Word template 2.0

(row 1 Figure 7), waters cannot cross the shelf edge so effectively, so even when the winds push warm waters onto the outer shelf they do not get to the Ice Front. The deep ocean gyre's importance is readily seen by comparing the δ_{wall} simulations (Figure 7 row 4) with the other boundary conditions (Figure 7 rows 1-3), the δ_{wall} simulations have a zonal structure and temperature variability with depth. The caveat is that the deep ocean gyre is only important when both the shelf *and* deep ocean is blocked (comparing Figure 7 rows 1,3 and rows 2-4). As compared to Figure 6, Figure 7 shows nuanced changes with the δ_{wall} simulations in terms of the zonal temperature structure (Figure 7 row 4). Figure 6 row 4 suggests that δ_{wall} removes any sensitivity to changes in wind stress; Figure 7 however shows zonal changes, namely, the bottom temperature intensifies with weaker easterlies and the bottom temperature is western intensified with stronger westerlies (Figure 7 bottom row). This is likely driven by the increase in southward meridional geostrophic transport highlighted in Section 2b.

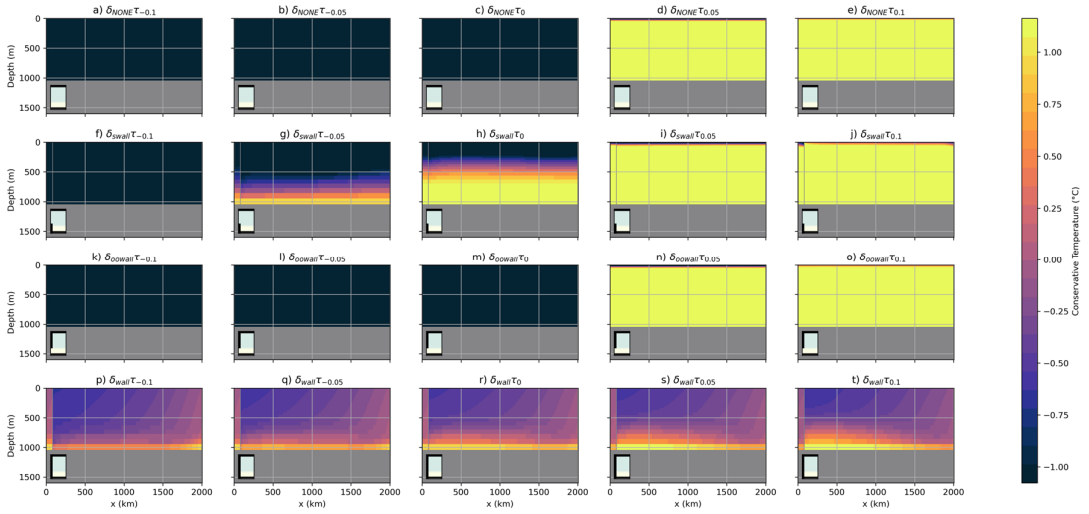

Figure 7. Same panel-experiment layout as Figure 6 but for southern boundary ("Ice Front" indicated Figure 5b) mean temperature.

File generated with AMS Word template 2.0

c *Understanding circulation changes due to winds and circulation regime*

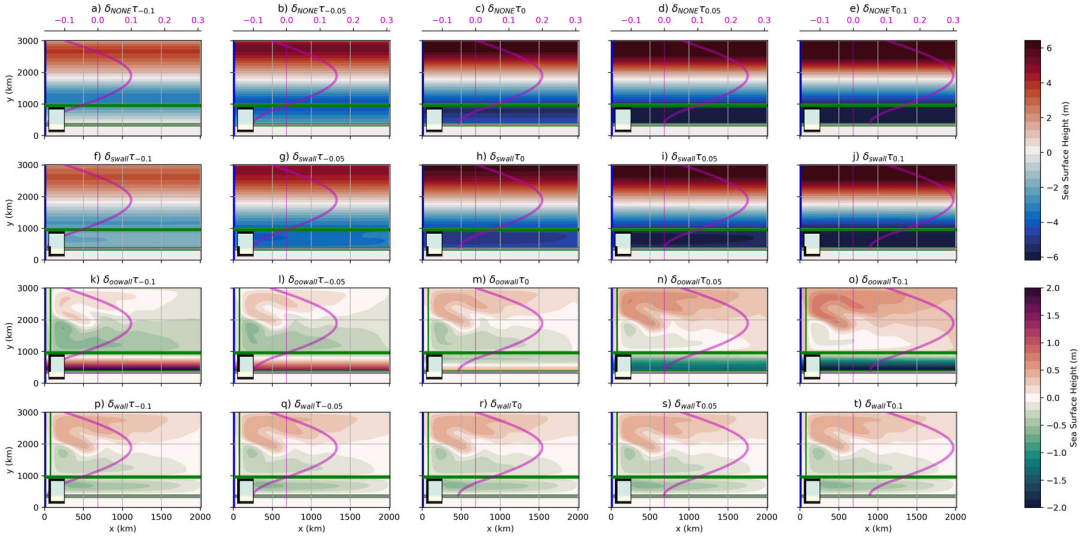

Figure 8. Same panel-experiment layout as Figure 6 but for sea surface height for all experiments. To compensate for large throughflow transports (Hidaka's dilemma; Hidaka & Tsuchiya, 1953) rows 1-2 (a-j) use a different colourbar to rows 3-4 (k-t). Thin green lines are isobaths.

Figures 8-11 summarize the horizontal and overturning circulation changes that lead to the described changes in temperature on the shelf. We consider horizontal circulation changes in terms of sea surface height (Figure 8-9) and the barotropic streamfunction (Figure 10). Figure 8-9 highlights how the near-surface geostrophic transport responds to changes in boundary conditions under the same top Ekman transport. A throughflow regime (top row Figure 8) is readily understood by considering the simpler case of when the stress is only eastward: $\delta_{NONE}\tau_{0.05}$ and $\delta_{NONE}\tau_{0.1}$ (Figure 8d-e) then, have a north-south SSH gradient, driven by northward Ekman transport that leads to an SSH maximum in the north and a minimum in the south (Figure S2d-e). The gradient is non-linear as the stress has curvature and f is varying. In contrast, $\delta_{NONE}\tau_{-0.05}$ and $\delta_{NONE}\tau_{-0.1}$ (Figure 8a-b), have two inflection points created from the introduction of a westward wind. Combining this view with the integrated transport in Figure 10, the strength and positions of the westward and eastward currents are modulated by the strength of the wind and the shift in location for the sign change in the winds.

File generated with AMS Word template 2.0

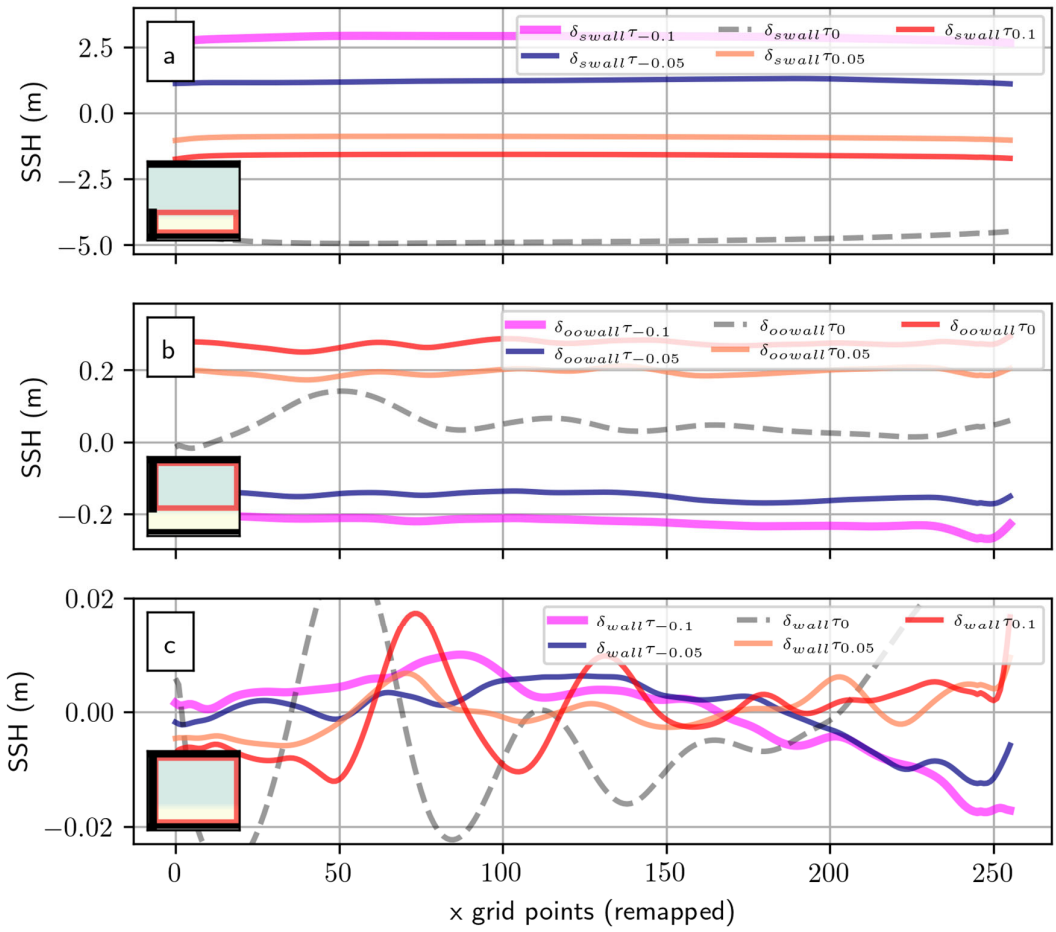

Figure 9. Sea surface height differences along x, across gyre regime experiments, solid lines show experiment – control, where control's raw values are shown in dashed gray line. For readability, the x-axis is remapped so that the x=1 is on the eastern side of the wall at 86km and the last point at x=257 is adjacent to the wall on the western side. a) δ_{swall} experiments with $\delta_{swall}\tau_0$ control; meridionally averaged over the shelf, b) δ_{oowall} experiments with $\delta_{oowall}\tau_0$ control; meridionally averaged over the deep ocean, c) δ_{wall} experiments with $\delta_{wall}\tau_0$ control; meridionally averaged over whole domain. The small glyphs schematically indicate the geometry and averaging region (red) under consideration in each panel. Note the y-axis changes in scale across the 3 panels.

Introducing a wall on the shelf (second row in Figure 8,10 and Figure 9a), the response in the deep ocean is the same as before but now with a gyre on the shelf. With a wall on the shelf, *sea surface height* on the shelf goes uniformly down with positive c (Figure 8i,j and 9a) and uniformly up with negative c (Figure 8f,g and 9a), this is due to the change in top Ekman transport with the change in c. With positive c, the top Ekman transport is northward over the shelf and increasingly stronger south with negative c. Similarly, introducing a wall in the deep ocean and changing the winds (third row in Figure 8, 10 and Figure 9b) leads to a clear change in the gyres in *sea surface height* in Figure 8. Specifically, as the easterlies get

File generated with AMS Word template 2.0

stronger (Figure 8k,l) the southern gyre gets larger as the southward top Ekman transport increases. Conversely, as the westerlies get stronger (Figure 8n,o), the top northward Ekman transport gets stronger and the northern gyre gets larger. Figure 9b shows that these SSH changes are mostly a uniform offset, this again can be explained by changes in top Ekman transports, see wall on the shelf case (above). As expected (see Section 2b), since it is the difference between contours that determines the transport in the streamfunction, the integrated circulation for the deep ocean gyres in Figure 10 is essentially unchanged across row 3; they look different as the barotropic streamfunction is calculated by integrating through the unblocked shelf first which has changed its transport, much like the shelf region in row 1. Finally, since the wind stress curl is unchanged, unsurprisingly, the barotropic streamfunction is unchanged in the full gyre regime experiments (bottom row Figure 10). Also as expected from Section 2b, the sea surface height does raise and lower as the strength of the offset is increased and decreased, respectively, see Figure 9c. The above described changes in Ekman transport and SSH are corroborated by commensurate changes in the zonal mean SSH (Figure S2).

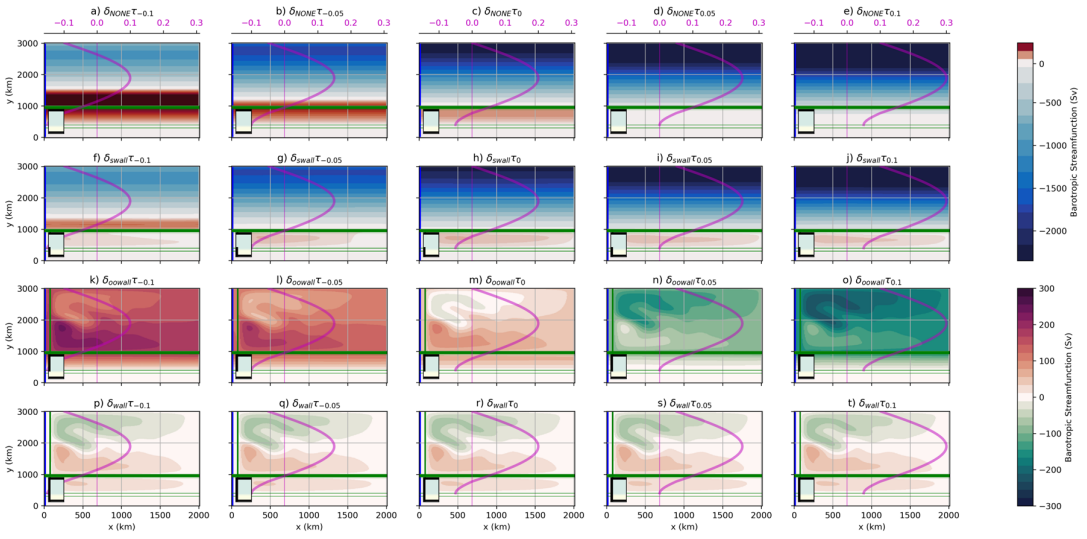

Figure 10. Same panel-experiment layout as Figure 6 but now the Barotropic Streamfunction for all experiments. To compensate for large throughflow transports, rows 1-2 use a different colourbar to rows 3-4. Thin green lines are isobaths.

The Eulerian meridional overturning streamfunctions shown in Figure 11 highlights how each boundary condition alters the means by which the vertical structure compensates for the

File generated with AMS Word template 2.0

changes in top Ekman transport as the stress changes. At the large scale, the overturning is throughflow dominant with boundary condition δ_{NONE}, δ_{swall} (rows 1-2 Figure 11), and gyre dominant for δ_{oowall} and δ_{wall} (rows 3-4 Figure 11). Across all regimes, the change in the direction of the top Ekman transport coincides with the latitude at which the winds change direction. In a fully throughflow regime (top row Figure 11), the northern (Figure 11a-e) and southern (Figure 11a-c) overturning cells, are modulated by the position and strength of the westerlies/easterlies, and the transition zone of the westerlies to easterlies (Figure 11a-c). This highlights how the change in upwelling up the shelf break occurs, driving the discussed shelf temperature changes (Section 4b; Figure 6). Introducing a wall on the shelf (row 2 Figure 11), the overturning is similar to δ_{NONE} (row 1 Figure 11) except that the return flow on the shelf is no longer confined to the bottom Ekman layer but is higher up in the water column as a geostrophic return flow, this makes the anti-clockwise cell on the shelf more baroclinic. Despite there being no westward wind in Figure 11i-j, there is a weak, sub-surface anti-clockwise overturning cell on the shelf, this is likely a closure for the now opposing zonal flows and the geostrophic return flow created by the gyre on the shelf. The deep ocean wall simulations δ_{oowall} (row 3 Figure 11) are readily understood by considering the δ_{wall} case and the above arguments. Introducing a full north-south wall (Figure 11r) leads to three gyres and their associated overturning (see Section 4a). As the winds are modified, e.g., with uniform westward wind (Figure 11p,q), the anti-clockwise cells above 1000m get larger and stronger. This is due to the increase in southward top Ekman transport at the southern boundary and the now southward top Ekman transport at the northern boundary. Similarly, with a uniform addition of eastward wind (Figure 11s,t), the near-surface clockwise-overturning cell gets larger and stronger. Re-visiting Figure 6 but now with the control simulations removed (middle $c = 0$ column), Figure S1 shows that the zonally averaged temperature does change in a consistent, modest way with these overturning changes. The observed linking of the bottom and top overturning cells in Figure 11s-t, likely also explains the modest temperature changes seen in δ_{oowall} row 4 in Figure 7. Here, we have only shown the Eulerian overturning, based on *Stewart and Thompson* (2012), since we have non-zero Easterlies at the Southern boundary we expect the eddy overturning to be small on the shelf and as the response to surface forcing change is linear (next Section), we do not expect large eddy overturning changes (across the rows of Figure 11).

File generated with AMS Word template 2.0

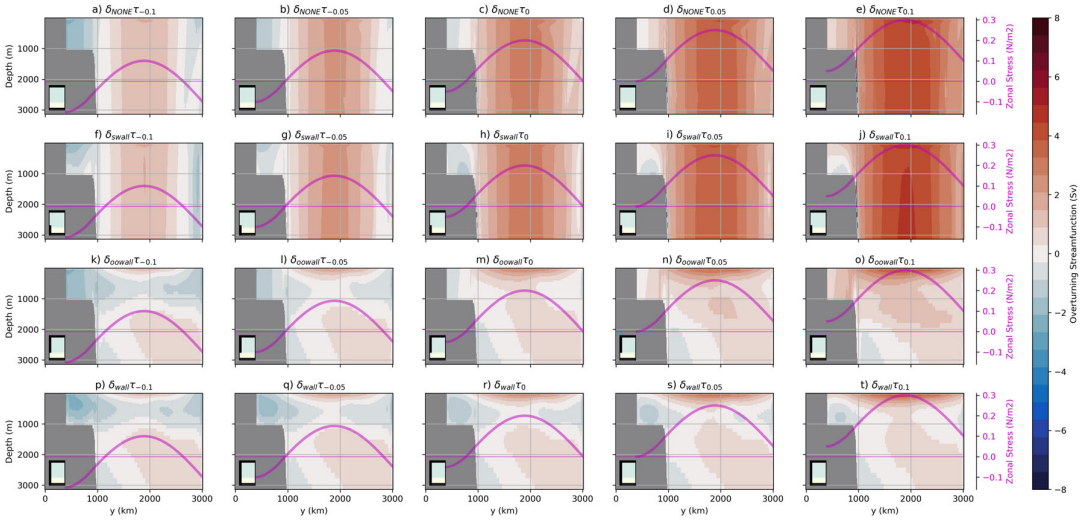

559

560 Figure 11. Same panel-experiment layout as Figure 6 but now the Meriodinal Overturning
561 Streamfunction for all experiments.

562 *d Momentum budget*

563 Several studies have found that eddies are a critical feature for fluxing heat and mass
564 across the shelf break (Stern et al., 2015; Stewart & Thompson, 2015; St-Laurent et al.,
565 2013). Throughout this study we have assumed that the changes in shelf temperatures
566 are largely a result of momentum advection from circulation changes. Here, using depth
567 and zonally integrated momentum budgets, we look to test whether these circulation
568 changes are indeed linear (not related to eddies) and that the described geostrophic and
569 Ekman dynamics (Section 2 and 4c) are what is driving those changes. The NEMO vector
570 invariant form of the momentum equation is:

571 $$\frac{\partial \boldsymbol{u}_h}{\partial t} = -\left[(\nabla \times \boldsymbol{u}) \times \boldsymbol{u} + \frac{1}{2}\nabla \boldsymbol{u}^2\right]_h - f\,(k \times \boldsymbol{u})_h - \frac{1}{\rho_0}\nabla_h P + D^u + F^u$$

572 where f is the Coriolis parameter, $\boldsymbol{u}_h$ is the horizontal velocity vector, ∇ and ∇_h is
573 the 3D and 2D gradient operators, respectively. $[\cdot]_{\boldsymbol{h}}$ is the horizontal component of a
574 vector. F^u is the vertical divergence of the vertical diffusive momentum fluxes, i.e.
575 $\frac{\partial}{\partial z}(\kappa_z \frac{\partial \boldsymbol{u_h}}{\partial z})$ which includes the top and bottom stress where $\int_{-H}^{\eta} F^u dz = \tau_s - \tau_b$. D^u is the
576 horizontal divergence of the horizontal diffusive momentum flux (i.e. $\nabla \cdot (\kappa_h \frac{\partial \boldsymbol{u_h}}{\partial x} +$
577 $\kappa_h \frac{\partial \boldsymbol{u_h}}{\partial y})$), with the turbulent horizontal (κ_h) and vertical (κ_Z) viscosities.

578

File generated with AMS Word template 2.0

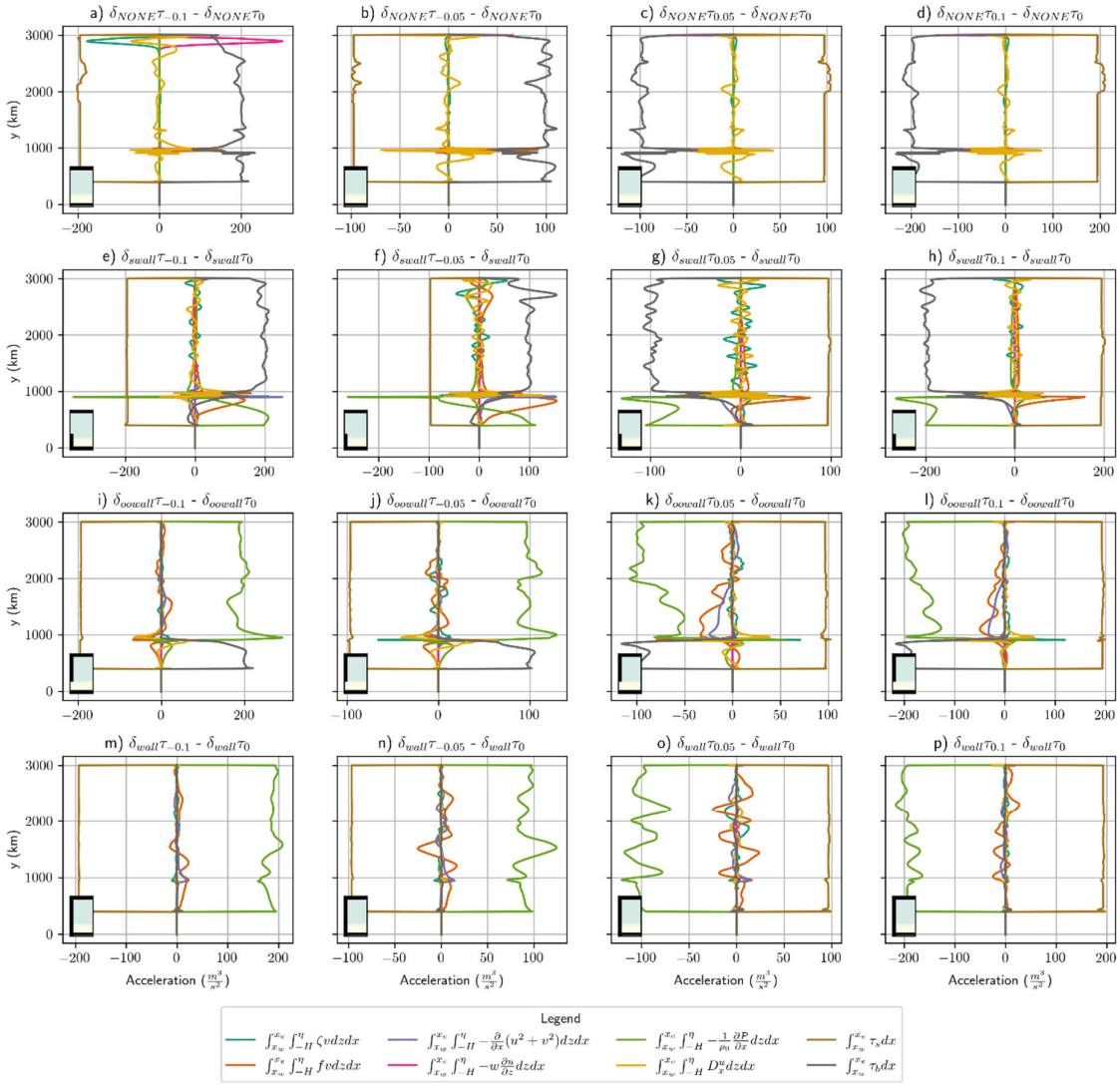

Figure 12. The 20 year time-average vertically and zonally integrated zonal momentum budget with control wind experiment removed. The terms are as described in Section 4.4 and indicated by the legend. Each row has a different boundary condition, in order: i) fully re-entrant, ii) blocked shelf, iii) blocked deep ocean and iv) fully blocked shelf and deep ocean, respectively. The small glyphs (bottom-left) schematically indicate the geometry under consideration in each panel.

Figure 12 shows the depth and zonally integrated x-momentum balance with the control wind stress for their respective boundary condition removed. As the control wind stress is removed, Figure 12-13 are primarily intended to be compared along the rows (Figure S4 and S5 show the respective raw values). Under a change in wind forcing, over a long time-mean ($\frac{\partial \boldsymbol{u}_h}{\partial t} = 0$), Figure 12 highlights the importance of bottom

File generated with AMS Word template 2.0

591 friction and pressure gradients in balancing the input of momentum by the wind stress.
592 In other words, unsurprisingly, the following terms dominate:

593 $$\int_{x_w}^{x_e} \tau_s \, dx = \underbrace{\int_{x_w}^{x_e} \tau_b \, dx}_{throughflow} + \underbrace{\int_{x_w}^{x_e} \int_{-H}^{\eta} \frac{\partial p}{\partial x} dz dx}_{gyre}$$

594 In regions where there is a throughflow regime (rows 1-3), the change in surface stress
595 $\int_{x_w}^{x_e} \tau_s \, dx$ (light brown) is matched by a commensurate and opposite change in bottom stress
596 $\int_{x_w}^{x_e} \tau_b \, dx$ (dark grey), along each row that is: over the whole domain, in the deep ocean and
597 on the shelf for rows 1-3, respectively. In contrast, in regions where there is a gyre regime
598 (rows 2-4), consistent with previous studies (D. R. Munday et al., 2015; Olbers et al., 2007),
599 the change in surface stress $\int_{x_w}^{x_e} \tau_s \, dx$ (light brown), is matched by a commensurate and
600 opposite change in the depth and zonally integrated pressure gradient $\int_{x_w}^{x_e} \int_{-H}^{\eta} \frac{\partial p}{\partial x} dz dx$ (i.e.
601 continental/topographic form stress), along each row that is: on the shelf, in the deep ocean
602 and over the whole domain for rows 2-4, respectively.
603

File generated with AMS Word template 2.0

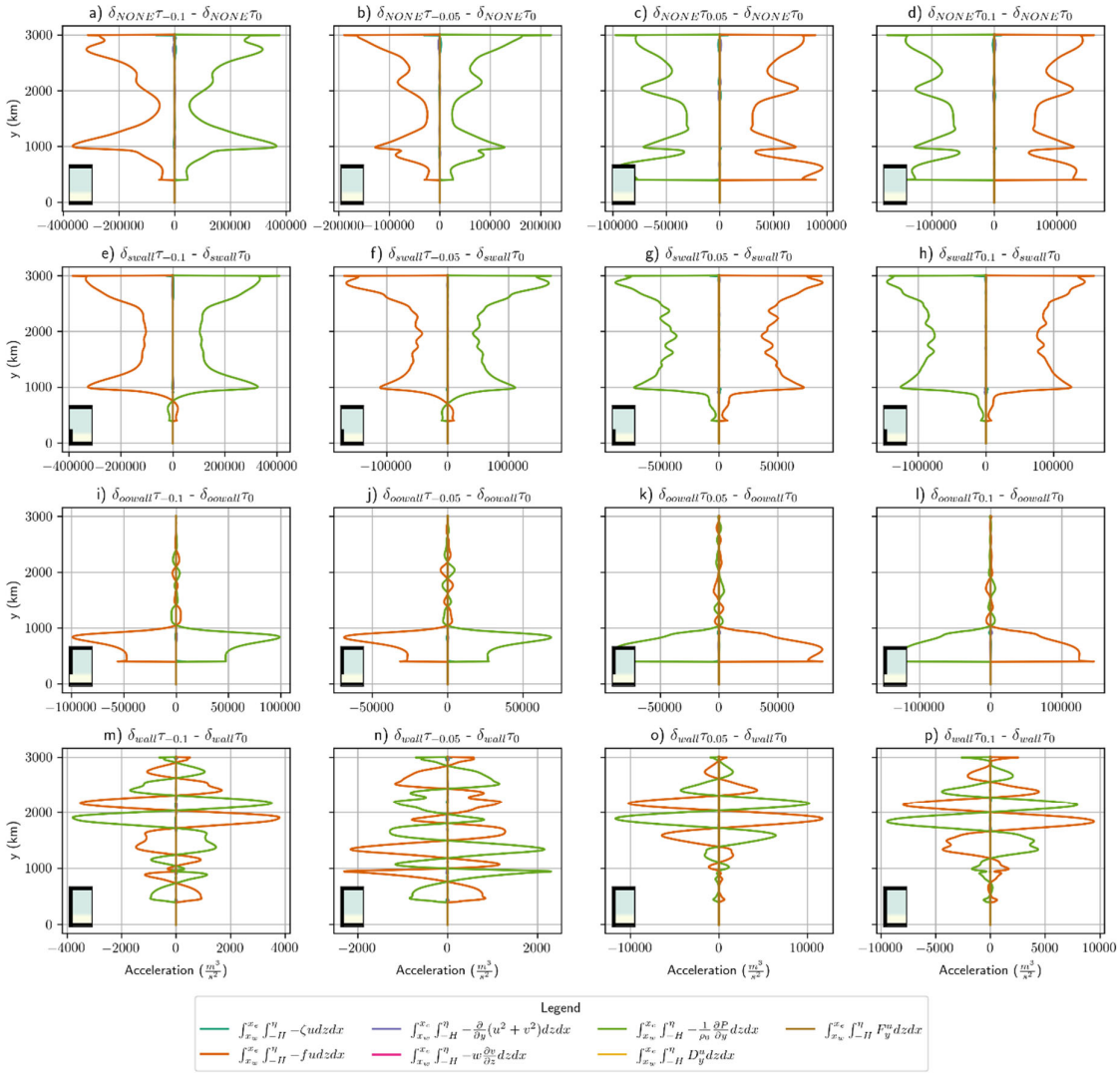

Figure 13. Same as Figure 12 but for the zonally integrated meridional momentum budget with control wind experiment removed.

Figure 13 shows the depth and zonally integrated y-momentum balance with the control wind stress experiment removed (Figure S5 shows the raw values). For context, recall that these simulations have no meridional stress and Figure S3 shows that the zonally averaged currents co-locate with the raw $\int_{x_w}^{x_e}\int_{-H}^{\eta} fu\, dz\, dx$ values of Figure S5. Here, under a change in wind forcing (comparing across the rows), over a long time-mean ($\frac{\partial \boldsymbol{u}_h}{\partial t} = 0$), Figure 12 highlights the importance of geostrophy, namely $\int_{x_w}^{x_e}\int_{-H}^{\eta} fu\, dz\, dx = -\frac{1}{\rho_0}\int_{x_w}^{x_e}\int_{-H}^{\eta} \frac{\partial p}{\partial y} dz dx$ where the change in the remaining terms is negligible. As the zonal momentum input from the wind changes across the rows in

Figure 13, this changes the strength of the zonal flow in the throughflow regimes where a pressure gradient compensates (rows 1-3). In particular, within rows 1-3, columns 1-2 have weaker winds, so the zonal currents decelerate, whereas columns 3-4 have stronger winds, so the zonal currents accelerate. As discussed earlier, there are small changes in the horizontal circulation in a fully gyre regime (row 4) which is why we see relatively small changes in geostrophic balance (note x-axis reduction in scale in row 4).

5 Summary and Discussion

In this study, we have explored how basin geometry and wind shifts have a large role in determining the temperature structure on Antarctica's shelf seas, furthermore, the basin geometry influences how susceptible the shelf temperatures are to changes in winds in the future.

We have used a simple barotropic model (Stommel's planetary geostrophic equations in Section 2), to explore the linear dynamical balances that change when the circulation regime changes from a channel to a gyre, we also examined how the Ekman and geostrophic circulations respond to changes in surface forcing within these two regimes, all in the absence of baroclinicity and topography. We then used the primitive equation ocean model NEMO (Section 4) with varying temperature to see if the barotropic arguments from Section 2 could explain the more complex circulation changes (Section 4c). Despite the NEMO model configuration used here including complications such as bathymetry and baroclinicity, we find that the time-mean results are largely understood by the simple barotropic model. In the simple model, we considered Ekman layers and geostrophic transports diagnostically, all three layers were within one slab of fluid whereas in NEMO, the described layers are now in separate fluid layers. Fundamentally, the time-mean equilibrated differences between the geometries and winds, can be understood by changes in the Ekman layers and a geostrophic circulation compensating for changes in boundary and surface stress induced top Ekman layer transport (Section 2b-c and 4c). Specifically, irrespective of boundary condition, from a zonally integrated perspective, the westerly and easterly stresses create a near surface northward and southward transport in the top Ekman layer, respectively. As we discuss in Section 2 and Section 4, the interior responds to these transports where the boundary condition determines how the response is constrained. In brief, we summarise the response as

File generated with AMS Word template 2.0

follows. In the case of a throughflow, as the easterly-westerly wind transition moves south, so does the confluence region in the bottom layers, and critically, the upwelling region that brings warm waters onto the shelf. We note that these results are consistent with more realistic simulations in the Amundsen Sea (Caillet et al., 2023; Haigh et al., 2023). In a gyre regime, when a wall is introduced, the return flow is no longer confined to the frictionally balanced bottom Ekman layers but rather a wall creates topographic form stress enabling a geostrophic return flow at every depth where the wall is present. We noted that the introduction of a deep ocean wall (Figure 6) led to the flattening of isotherms in the deep ocean, with less warm waters close to the shelf. Applying the above arguments, we see this is because the return flow set up by the near-surface Ekman transport is more evenly distributed throughout the water column whereas when the return flow is in the frictionally balanced bottom Ekman layer. Whilst these largely linear dynamics balance have been understood for some time (e.g. *Veronis* (1996) and *Vallis* (2017)), we think this is the first time they have been re-visited in terms of Antarctic shelf temperatures in a realistic primitive equation ocean model.

When it comes to understanding future Southern Ocean projections, from the gyre regime simulations with a constant offset in the winds, we think this work demonstrates that we need to diagnose how the winds change, i.e. strength, a latitudinal shift, a change in curl as this allows us to manage our expectations for the change we expect. Despite several studies focuses on eddies as a critical feature for fluxing heat and mass across the shelf break (Stern et al., 2015; Stewart & Thompson, 2015; St-Laurent et al., 2013), in this instance, NEMO's momentum budget shows that over equilibrated timescales, the system response to *surface forcing changes* is first-order linear (some geometry changes, e.g., Figure 7c,h and S4c,h involve non-linear advection). The linear nature of the surface forcing response may be because of the focus on equilibrated changes and the relatively coarse resolution of the model (7.9 km); *Stewart and Thompson* (2015) found that 1km or finer is required to resolve the eddies for cross-shelf heat transport. However, on the larger scale, Stewart and Thompson (2012) found that 5 km was sufficient to resolve the Easterly eddy overturning on the shelf. Future work, could re-visit these problems with finer resolution. Furthermore, while these simulations lack many important features (e.g., buoyancy forcing changes, varying forcing, sea ice, ice shelves, meridional winds, realistic bathymetry et cetera) we hope this study

File generated with AMS Word template 2.0

679 encourages others to consider basin geometry and easterlies in related idealized studies; our
680 own work is ongoing in adding other features.

681

682 A remaining question is how the simplest of geometries and forcing considered here is
683 relevant to the real ocean. To manage expectations, as winds change, we need metrics to
684 diagnose when we are in a gyre or throughflow regime, blocked f/h contours offer some
685 barotropic insight here but the mechanisms described in this paper apply in partial cases too.
686 In this study, we intentionally made the transitions distinct, making the diagnostics simple
687 (Section 4d) but in the real Southern Ocean the dynamics is more mixed. Indeed, Masich et
688 al. (2015) found that 95% of the momentum input by the wind at ACC latitudes is balanced
689 by topographic form stress, reinforcing that the real Southern Ocean is very different to the
690 idealized flat bottomed channels discussed here. We thus need a stratification dependent
691 metric to diagnose the degree to which a region is in a channel or gyre regime. We think
692 work such as Figure 5 from *Waldman and Giordani* (2022) diagnosing the dominant vorticity
693 balance in different regions is work in the right direction. We assume this kind of diagnostic
694 would need to reconcile throughflow and gyre dynamics into a singular framework,
695 considerable discussion has occurred on this topic (Hughes, 2000, 2002; Hughes & Cuevas,
696 2001; Jackson et al., 2006; Olbers, 1998; Olbers et al., 2004; Warren et al., 1996). On
697 applying Sverdrup theory in the Southern Ocean, *Hughes* (2002) used Sverdrup like theories
698 from (Stommel, 1957; Webb, 1993) to estimate ACC transport, see (LaCasce & Isachsen,
699 2010) for a more general review of linear theories. For vorticity in gyres alone, direct
700 buoyancy forcing aside, the dominant terms are still debated. For example, *Hughes* (2000)
701 notes that the historical tendency to focus on gyres in boxes with straight walls (Walter H.
702 Munk, 1950; Stommel, 1948) has led to the view that the return flow in western boundary
703 currents occurs due to friction and viscosity. In reality, coastlines are sloped, leading to
704 inviscid western currents where, like the channel regime, the wind stress is balanced by
705 topographic form stress, or in vorticity parlance bottom pressure "torques" balance the wind
706 stress curl (e.g. Schoonover et al., 2017; Styles et al., 2021). Here, we are interested in heat
707 transport across Antarctica's shelf break, if we think of this in terms of momentum transport
708 across f/h contours then the above theories highlight (for vorticity), that momentum
709 transport across a sloping shelf break or bottom ridge requires an additional source of
710 vorticity, and the kind of dissipation (e.g. Munk, Stommel et cetera) changes depending on

File generated with AMS Word template 2.0

711 the nature of the feature. If we are to understand how Antarctica's shelf temperatures will
712 respond to a warming climate, then further work is needed on how to apply these ideas across
713 mixed flow regimes.

714 *Acknowledgments.*

715 This work used the ARCHER2 UK National Supercomputing Service
716 (https://www.archer2.ac.uk). C.B. and A. J. are supported by the European Union's Horizon
717 2020 research and innovation programme under grant agreement no. 820575 (TiPACCs). For
718 the purpose of Open Access, the author has applied a CC BY public copyright licence to any
719 Author Accepted Manuscript (AAM) version arising from this submission. C.B. gratefully
720 acknowledges Paul Holland for asking *the* question and Andrew Kiss for a 2014 lecture on
721 western boundary currents, the start of the journey. We thank Dave Storkey for his work on
722 the momentum trend budgets (branch below).

723 *Data Availability Statement.*

724 Key NEMO configuration files and model outputs will be made available on Zenodo
725 following final revisions of this article. The NEMO configuration used in this article uses
726 NEMO version 4.0.4 with the following branch:
727 branches/UKMO/NEMO_4.0.4_momentum_trends @ 15194. This branch can be found on
728 the (old svn) repository at: https://forge.ipsl.jussieu.fr/nemo/browser/NEMO/. The finite
729 element method solve for Stommel's planetary geostrophic equations in Section 2 used
730 Mathematica v13.2.

731 REFERENCES

732 Abernathey, R., Marshall, J., & Ferreira, D. (2011). The Dependence of Southern Ocean
733 Meridional Overturning on Wind Stress. *Journal of Physical Oceanography*, *41*(12).
734 https://doi.org/10.1175/JPO-D-11-023.1

735 Armitage, T. W. K., Kwok, R., Thompson, A. F., & Cunningham, G. (2018). Dynamic
736 Topography and Sea Level Anomalies of the Southern Ocean: Variability and
737 Teleconnections. *Journal of Geophysical Research: Oceans*, *123*(1), 613–630.
738 https://doi.org/10.1002/2017JC013534

739 Bracegirdle, T. J., Shuckburgh, E., Sallee, J.-B., Wang, Z., Meijers, A. J. S., Bruneau, N., et
740 al. (2013). Assessment of surface winds over the Atlantic, Indian, and Pacific Ocean
741 sectors of the Southern Ocean in CMIP5 models: historical bias, forcing response, and
742 state dependence: CMIP5 SOUTHERN OCEAN SURFACE WINDS. *Journal of*
743 *Geophysical Research: Atmospheres*, *118*(2), 547–562.
744 https://doi.org/10.1002/jgrd.50153

745 Caillet, J., Jourdain, N. C., Mathiot, P., Hellmer, H. H., & Mouginot, J. (2023). Drivers and
746 Reversibility of Abrupt Ocean State Transitions in the Amundsen Sea, Antarctica.
747 *Journal of Geophysical Research: Oceans*, *128*(1), e2022JC018929.
748 https://doi.org/10.1029/2022JC018929

749 Constantinou, N. C., & Hogg, A. McC. (2019). Eddy Saturation of the Southern Ocean: A
750 Baroclinic Versus Barotropic Perspective. *Geophysical Research Letters*, *46*(21),
751 12202–12212. https://doi.org/10.1029/2019GL084117

752 Donohue, K. A., Tracey, K. L., Watts, D. R., Chidichimo, M. P., & Chereskin, T. K. (2016).
753 Mean Antarctic Circumpolar Current transport measured in Drake Passage.
754 *Geophysical Research Letters*, *43*(22), 11,760-11,767.
755 https://doi.org/10.1002/2016GL070319

756 Dotto, T. S., Naveira Garabato, A., Bacon, S., Tsamados, M., Holland, P. R., Hooley, J., et al.
757 (2018). Variability of the Ross Gyre, Southern Ocean: Drivers and Responses
758 Revealed by Satellite Altimetry. *Geophysical Research Letters*.
759 https://doi.org/10.1029/2018GL078607

760 Farneti, R., Downes, S. M., Griffies, S. M., Marsland, S. J., Behrens, E., Bentsen, M., et al.
761 (2015). An assessment of Antarctic Circumpolar Current and Southern Ocean
762 meridional overturning circulation during 1958–2007 in a suite of interannual CORE-

II simulations. *Ocean Modelling*, *93*, 84–120. https://doi.org/10.1016/j.ocemod.2015.07.009

Gnanadesikan, A., & Hallberg, R. W. (2000). On the Relationship of the Circumpolar Current to Southern Hemisphere Winds in Coarse-Resolution Ocean Models. *Journal of Physical Oceanography*, *Volume 30*(Issue 8). Retrieved from https://journals.ametsoc.org/view/journals/phoc/30/8/1520-0485_2000_030_2013_otrotc_2.0.co_2.xml

Gómez-Valdivia, F., Holland, P. R., Siahaan, A., Dutrieux, P., & Young, E. (2023). Projected West Antarctic Ocean Warming Caused by an Expansion of the Ross Gyre. *Geophysical Research Letters*, *50*(6), e2023GL102978. https://doi.org/10.1029/2023GL102978

Goyal, R., Sen Gupta, A., Jucker, M., & England, M. H. (2021). Historical and Projected Changes in the Southern Hemisphere Surface Westerlies. *Geophysical Research Letters*, *48*(4), e2020GL090849. https://doi.org/10.1029/2020GL090849

Haigh, M., Holland, P. R., & Jenkins, A. (2023). The Influence of Bathymetry Over Heat Transport Onto the Amundsen Sea Continental Shelf. *Journal of Geophysical Research: Oceans*, *128*(5), e2022JC019460. https://doi.org/10.1029/2022JC019460

Hidaka, K., & Tsuchiya, M. (1953). On the Antarctic circumpolar current. *Journal of Marine Research*, *12*(2). Retrieved from https://elischolar.library.yale.edu/journal_of_marine_research/794

Hughes, C. W. (1997). Comments on “On the Obscurantist Physics of ‘Form Drag’ in Theorizing about the Circumpolar Current.” *Journal of Physical Oceanography*, *27*(1), 209–210. https://doi.org/10.1175/1520-0485(1997)027<0209:COOTOP>2.0.CO;2

787 Hughes, C. W. (2000). A theoretical reason to expect inviscid western boundary currents in
788 realistic oceans. *Ocean Modelling*, *2*(1), 73–83. https://doi.org/10.1016/S1463-
789 5003(00)00011-1

790 Hughes, C. W. (2002). Sverdrup-like theories of the Antarctic Circumpolar Current. *Journal*
791 *of Marine Research*, *60*(1), 1–17. https://doi.org/10.1357/002224002762341221

792 Hughes, C. W., & Cuevas, B. A. de. (2001). Why Western Boundary Currents in Realistic
793 Oceans are Inviscid: A Link between Form Stress and Bottom Pressure Torques.
794 *Journal of Physical Oceanography*, *31*(10), 2871–2885. https://doi.org/10.1175/1520-
795 0485(2001)031<2871:WWBCIR>2.0.CO;2

796 Jackson, L., Hughes, C. W., & Williams, R. G. (2006). Topographic Control of Basin and
797 Channel Flows: The Role of Bottom Pressure Torques and Friction. *Journal of*
798 *Physical Oceanography*, *36*(9), 1786–1805. https://doi.org/10.1175/JPO2936.1

799 LaCasce, J. H., & Isachsen, P. E. (2010). The linear models of the ACC. *Progress in*
800 *Oceanography*, *84*(3), 139–157. https://doi.org/10.1016/j.pocean.2009.11.002

801 Masich, J., Chereskin, T. K., & Mazloff, M. R. (2015). Topographic form stress in the
802 Southern Ocean State Estimate. *Journal of Geophysical Research: Oceans*, *120*(12),
803 7919–7933. https://doi.org/10.1002/2015JC011143

804 Meredith, M. P., Woodworth, P. L., Chereskin, T. K., Marshall, D. P., Allison, L. C., Bigg,
805 G. R., et al. (2011). Sustained Monitoring of the Southern Ocean at Drake Passage:
806 Past Achievements and Future Priorities. *Reviews of Geophysics*, *49*(4).
807 https://doi.org/10.1029/2010RG000348

808 Morrison, A. K., Hogg, A. M., & Ward, M. L. (2011). Sensitivity of the Southern Ocean
809 overturning circulation to surface buoyancy forcing: SOUTHERN OCEAN

OVERTURNING. *Geophysical Research Letters*, *38*(14), n/a-n/a. https://doi.org/10.1029/2011GL048031

Munday, D. R., Johnson, H. L., & Marshall, D. P. (2015). The role of ocean gateways in the dynamics and sensitivity to wind stress of the early Antarctic Circumpolar Current. *Paleoceanography*, *30*(3), 284–302. https://doi.org/10.1002/2014PA002675

Munday, David R., Johnson, H. L., & Marshall, D. P. (2013). Eddy Saturation of Equilibrated Circumpolar Currents. *Journal of Physical Oceanography*, *43*(3), 507–532. https://doi.org/10.1175/JPO-D-12-095.1

Munk, W H, & Palmen, E. (1951). Note on the Dynamics of the Antarctic Circumpolar Current, 3.

Munk, Walter H. (1950). On the wind-driven ocean circulation. *Journal of Meterology*. https://doi.org/10.1175/1520-0469(1950)007<0080:OTWDOC>2.0.CO;2

Neme, J., England, M. H., & Hogg, A. McC. (2021). Seasonal and Interannual Variability of the Weddell Gyre From a High-Resolution Global Ocean-Sea Ice Simulation During 1958–2018. *Journal of Geophysical Research: Oceans*, *126*(11), e2021JC017662. https://doi.org/10.1029/2021JC017662

Olbers, D. (1998). Comments on “On the Obscurantist Physics of ‘Form Drag’ in Theorizing about the Circumpolar Current. *Journal of Physical Oceanography*, *28*(8), 1647–1654. https://doi.org/10.1175/1520-0485(1998)028<1647:COOTOP>2.0.CO;2

Olbers, D., Borowski, D., Völker, C., & Wölff, J.-O. (2004). The dynamical balance, transport and circulation of the Antarctic Circumpolar Current. *Antarctic Science*, *16*(4), 439–470. https://doi.org/10.1017/S0954102004002251

832 Olbers, D., Lettmann, K., & Timmermann, R. (2007). Six circumpolar currents—on the
833 forcing of the Antarctic Circumpolar Current by wind and mixing. *Ocean Dynamics*,
834 *57*(1), 12–31. https://doi.org/10.1007/s10236-006-0087-9

835 Olbers, D., Willebrand, J., & Eden, C. (2012). *Ocean Dynamics*. Berlin, Heidelberg: Springer
836 Berlin Heidelberg. https://doi.org/10.1007/978-3-642-23450-7

837 Patmore, R. D., Holland, P. R., Munday, D. R., Naveira Garabato, A. C., Stevens, D. P., &
838 Meredith, M. P. (2019). Topographic Control of Southern Ocean Gyres and the
839 Antarctic Circumpolar Current: A Barotropic Perspective. *Journal of Physical*
840 *Oceanography*, *49*(12), 3221–3244. https://doi.org/10.1175/JPO-D-19-0083.1

841 Pauthenet, E., Sallée, J.-B., Schmidtko, S., & Nerini, D. (2021). Seasonal Variation of the
842 Antarctic Slope Front Occurrence and Position Estimated from an Interpolated
843 Hydrographic Climatology. *Journal of Physical Oceanography*, *51*(5), 1539–1557.
844 https://doi.org/10.1175/JPO-D-20-0186.1

845 Purich, A., & England, M. H. (2021). Historical and Future Projected Warming of Antarctic
846 Shelf Bottom Water in CMIP6 Models. *Geophysical Research Letters*, *48*(10).
847 https://doi.org/10.1029/2021GL092752

848 Schoonover, J., Dewar, W. K., Wienders, N., & Deremble, B. (2017). Local Sensitivities of
849 the Gulf Stream Separation. *Journal of Physical Oceanography*, *47*(2), 353–373.
850 https://doi.org/10.1175/JPO-D-16-0195.1

851 Spence, P., Griffies, S. M., England, M. H., Hogg, A. McC., Saenko, O. A., & Jourdain, N.
852 C. (2014). Rapid subsurface warming and circulation changes of Antarctic coastal
853 waters by poleward shifting winds: Antarctic subsurface ocean warming. *Geophysical*
854 *Research Letters*, *41*(13), 4601–4610. https://doi.org/10.1002/2014GL060613

File generated with AMS Word template 2.0

855 Spence, P., Holmes, R. M., Hogg, A. McC., Griffies, S. M., Stewart, K. D., & England, M. H.
856 (2017). Localized rapid warming of West Antarctic subsurface waters by remote
857 winds. *Nature Climate Change*, *7*(8), 595–603. https://doi.org/10.1038/nclimate3335

858 Stern, A., Nadeau, L.-P., & Holland, D. (2015). Instability and Mixing of Zonal Jets along an
859 Idealized Continental Shelf Break. *American Meteorological Society*. Retrieved from
860 https://dspace.mit.edu/handle/1721.1/102085

861 Stewart, A. L. (2021). Warming spins up the Southern Ocean. *Nature Climate Change*, 1–2.
862 https://doi.org/10.1038/s41558-021-01227-y

863 Stewart, A. L., & Thompson, A. F. (2012). Sensitivity of the ocean's deep overturning
864 circulation to easterly Antarctic winds. *Geophysical Research Letters*, *39*(18).
865 https://doi.org/10.1029/2012GL053099

866 Stewart, A. L., & Thompson, A. F. (2015). Eddy-mediated transport of warm Circumpolar
867 Deep Water across the Antarctic Shelf Break. *Geophysical Research Letters*, *42*(2),
868 432–440. https://doi.org/10.1002/2014GL062281

869 Stewart, A. L., McWilliams, J. C., & Solodoch, A. (2021). On the Role of Bottom Pressure
870 Torques in Wind-Driven Gyres. *Journal of Physical Oceanography*, *51*(5), 1441–
871 1464. https://doi.org/10.1175/JPO-D-20-0147.1

872 St-Laurent, P., Klinck, J. M., & Dinniman, M. S. (2013). On the Role of Coastal Troughs in
873 the Circulation of Warm Circumpolar Deep Water on Antarctic Shelves. *Journal of*
874 *Physical Oceanography*, *43*(1), 51–64. https://doi.org/10.1175/JPO-D-11-0237.1

875 Stommel, H. (1948). The westward intensification of wind-driven ocean currents.
876 *Transactions, American Geophysical Union*, *29*(2), 202.
877 https://doi.org/10.1029/TR029i002p00202

878 Stommel, H. (1957). A survey of ocean current theory. *Deep Sea Research (1953)*, *4*, 149–
879 184. https://doi.org/10.1016/0146-6313(56)90048-X

880 Straub, D. N. (1993). On the Transport and Angular Momentum Balance of Channel Models
881 of the Antarctic Circumpolar Current. *Journal of Physical Oceanography*, *23*(4), 776–
882 782. https://doi.org/10.1175/1520-0485(1993)023<0776:OTTAAM>2.0.CO;2

883 Styles, A., Bell, M., Marshall, D., & Storkey, D. (2021, October 28). Spurious forces can
884 dominate the vorticity budget of ocean gyres on the C-grid [preprint].
885 https://doi.org/10.1002/essoar.10508527.1

886 Tansley, C. E., & Marshall, D. P. (2001). On the Dynamics of Wind-Driven Circumpolar
887 Currents. *Journal of Physical Oceanography*, *31*(11), 3258–3273.
888 https://doi.org/10.1175/1520-0485(2001)031<3258:OTDOWD>2.0.CO;2

889 Thompson, A. F., Stewart, A. L., Spence, P., & Heywood, K. J. (2018). The Antarctic Slope
890 Current in a Changing Climate. *Reviews of Geophysics*, *56*(4), 741–770.
891 https://doi.org/10.1029/2018RG000624

892 Vallis, G. K. (2017). *Atmospheric and Oceanic Fluid Dynamics: Fundamentals and Large-*
893 *Scale Circulation* (2nd ed.). Cambridge: Cambridge University Press.
894 https://doi.org/10.1017/9781107588417

895 Verfaillie, D., Pelletier, C., Goosse, H., Jourdain, N. C., Bull, C. Y. S., Dalaiden, Q., et al.
896 (2022). The circum-Antarctic ice-shelves respond to a more positive Southern
897 Annular Mode with regionally varied melting. *Communications Earth &*
898 *Environment*, *3*(1), 1–12. https://doi.org/10.1038/s43247-022-00458-x

899 Veronis, G. (1996). Effect of a Constant, Zonal Wind on Wind-Driven Ocean Circulation.
900 *Journal of Physical Oceanography*, *26*(11), 2525–2528. https://doi.org/10.1175/1520-
901 0485(1996)026<2525:EOACZW>2.0.CO;2

902 Waldman, R., & Giordani, H. (2022). Ocean barotropic vorticity balances: theory and
903 application to numerical models, *Authorea*. https://doi.org/10.1002/essoar.10511808.1

904 Warren, B. A., LaCasce, J. H., & Robbins, P. E. (1996). On the Obscurantist Physics of
905 "Form Drag" in Theorizing about the Circumpolar Current. *Journal of Physical*
906 *Oceanography*, *26*(10), 2297–2301. https://doi.org/10.1175/1520-
907 0485(1996)026<2297:OTOPOD>2.0.CO;2

908 Webb, D. J. (1993). A simple model of the effect of the Kerguelen Plateau on the strength of
909 the Antarctic Circumpolar Current. *Geophysical & Astrophysical Fluid Dynamics*,
910 *70*(1–4), 57–84. https://doi.org/10.1080/03091929308203587

911 Whitworth, T., Orsi, A. H., Kim, S.-., Nowlin, W. D., & Locarnini, R. A. (1998). Water
912 masses and mixing near the Antarctic Slope Front. In S. S. Jacobs & R. F. Weiss
913 (Eds.), *Ocean, ice, and atmosphere: interactions at the Antarctic continental margin*
914 (Vol. 75, pp. 1–27). American Geophysical Union.

915 Wilson, E. A., Thompson, A. F., Stewart, A. L., & Sun, S. (2021). Bathymetric control of
916 subpolar gyres and the overturning circulation in the Southern Ocean. *Journal of*
917 *Physical Oceanography*, *1*(aop). https://doi.org/10.1175/JPO-D-21-0136.1

918